Seismic Signatures of fluid pathways along the southern flank of the Asse salt structure

Master's thesis of

Lenny Yadhira Mejia Mendez

at the Geophysical Institute (GPI)
KIT-Department of Physics
Karlsruhe Institute of Technology (KIT)

Date of submission:
01.03.2024

Supervisor:	Prof. Dr. Thomas Bohlen
Co-supervisor:	Prof. Dr. Stefan Buske
Advisor:	Dr. Lars Houpt
Co-advisor:	Dr. Thomas Hertweck

Erklärung / Statutory declaration

Ich versichere wahrheitsgemäß, die Arbeit selbstständig verfasst, alle benutzten Hilfsmittel vollständig und genau angegeben und alles kenntlich gemacht zu haben, was aus Arbeiten anderer unverändert oder mit Abänderungen entnommen wurde sowie die Satzung des KIT zur Sicherung guter wissenschaftlicher Praxis in der momentan gültigen Fassung beachtet zu haben.

I declare truthfully that I have written this thesis all by myself, that I have fully and accurately specified all auxiliary means used, that I have correctly cited (marked) everything that was taken, either unchanged or with modification, from the work of others, and that I have complied with the current version of the KIT statutes for safeguarding good scientific practice.

Karlsruhe, 01.03.2024

Signature: Lenny Yadhira Mejia Mendez

Abstract

From 1967 to 1978, nuclear waste was deposited in the former salt and potash mine Asse II in Lower Saxony. Since 1988, fluids inflow and structural instabilities have occurred and pose risks to the secure storage of the nuclear waste. In response, the German parliament decided in 2013 to abandon this nuclear repository. For the safe retrieval of the radioactive waste and construction of a new shaft, a detailed understanding of the geological structure of the Asse is required. In 2020, the operator Bundesgesellschaft für Endlagerung (BGE) therefore acquired new high-quality 3D seismic data.

As the fluids inflow plays a crucial role regarding the integrity of the repository, this study investigates details of the Asse geology along the southern flank of the salt structure, which is associated with potential fluid pathways. The prevailing hypothesis suggests that fluids travel from the top of the salt dome to the mine's ingress point through the fractured Röt-Anhydrite-B formation, which has a thickness of about 16 meters. Using forward modeling, we could study where changes of this formation would show up at the surface in the recorded seismic data. Furthermore, To understand the influence of the Röt-Anhydrite-B formation on the seismic data, several geological models were built and used to simulate seismic data by finite-difference modelling.

This allowed us to study the influence of changes in various properties such as, for instance, the layer's wave propagation velocities, density, or thickness, leading to changes in the reflection coefficients or tuning and scattering effects. In a final stage, migrated field data were analyzed and checked for potential signatures that resemble effects seen in the synthetic studies.

With this comprehensive approach we were able to identify characteristics of changes in the critical angle, amplitudes and waveforms varying with the alteration of the parameters of the anhydrite layer. An expected decrease in the velocity and density in this formation due to fractures results in an increased critical angle and a decrease in the amplitude of the reflection coefficient prior to reaching the critical angle. From the modelled tuning effects, we can infer the thickness of the anhydrite layer. And from the analysis of the field data at different dip angles and frequencies we found that the anhydrite reflector was better trackable within dip angles ranging from 0° to 5° and frequency ranges from 10 Hz to 50 Hz.

List of Figures

List of Tables

Contents

Chapter 1

Introduction

The Asse-Heeseberg is an anticlinal structure, located in Lower Saxony near Remlingen, in the Subhercynian Basin (SB), which is part of the North German Basin (NGB) and sits within the northern foreland of the Harz mountains. This prominent geological feature is approximately eight kilometers in length and up to two kilometers in width, dominated by the Asse hill standing at an elevation of 234 meters above sea level. The NW-SE-oriented Asse hill is divided into the southern and northern flanks, stretching from Groß Denkte through the Asse I and Asse II shafts towards Klein Vahlberger (Fig. 1.1). The terrain showcases gentle slopes and occasional steeper ruptures, particularly towards the southwest.

Figure 1.1: *The Asse-Heeseberg Hill (Google, 2024).*

The anticline salt structure is formed by evaporite successions from the Zechstein group in the Late Permian. These rocks, up to 1500 meters thick, have undergone various tectonic impacts, evolving from flat bedded formations to a salt dome during the Jurassic and experiencing compressional tectonics in the Late Cretaceous; the Asse salt structure, mainly consisting of mobile rock salt from the Staßfurt-Formation, exhibits complex outer shapes and internal compositions (Pollok et al., 2018).

The sedimentary overburden mainly consists of Lower Buntsandstein, exhibiting diverse features like fossil-rich limestones and evaporites. As the Staßfurt-Formation pierced through the Triassic overburden during the rise of the salt structure, the Middle and Lower Buntsandstein layers sheared off along the salt rock and penetrated the core of the

salt structure in the north-eastern flank. On the southwestern flank of the structure, the evaporites of the upper Buntsandstein conform the overburden, which is in contact with the Zechstein. This flank presents the more steeply-sloping and heavily faulted structure (Szymaniak and Schäfer, 2002).

The geological units Buntsandstein, Muschelkalk (Middle Triassic), and Keuper (Upper Triassic) are at the top of the central salt structure. They are severely faulted and sharply asymmetrically dipping, with the northern flank being between 40° and 60° and the southern side being above 70° (Saßnowski et al., 2018). The complex geological nature of the Asse salt structure poses significant challenges in creating a detailed subsurface model from seismic data due to the complex wavefields generated by high-contrast interfaces and substantial topographical changes. Furthermore, fluid inflows in the area influence the imaging of the seismic data.

The Asse II mine was built in the early 20th century to extract rock salt and potash salt. It operated between 1909 and 1964, with excavation reaching depths from -490 m to a maximum of -775 m, resulting in 131 mining chambers. While potash salt chambers at the northern flank were backfilled after use, approximately 3,500,000 m^3 of empty volume generated from rock salt mining remained open for decades on the southern side. After mining ended, the German Federal Government acquired the mine, repurposing it as a nuclear waste repository. Between 1967 and 1978, it stored 125,787 barrels of low-level and intermediate-level radioactive waste. Thirteen former mining chambers were selected for waste placement, distributed across three levels (511 m level, 725 m level and 750 m level). Chamber 7, situated at the 725-meter level, remains accessible and offers insights into its condition, emplacement technology, and back-filling (Pollok et al., 2018; Sortan, 2022). Additionally, a research facility was established below the 800-meter level post-closure to Assess the suitability of salt for storing heat-generating radioactive waste, with research conducted from 1987 to 1995.

Currently, the Asse II mine presents notable issues: saline solutions from the Mesozoic overburden infiltrate the mine at a rate of 12.5 m^3/d. Simultaneously, stability concerns arise due to convergence problems within the mine openings caused by extensive open drifts and mining districts. In 2009, the Federal Office for Radiation Protection (BfS) took over control to promptly decommission the Asse II mine under atomic law. After reviewing three options, the government, considering long-term safety needs and available knowledge, concluded in 2010 that the safe decommissioning of the mine would only be viable after retrieving waste from its depths (Pollok et al., 2018).

1.1 Fluids in the Asse II mine (compilation of prior studies)

Since the late 1980s, it has been widely acknowledged that fluid inflow has been detected on the southern flank of the Asse II salt mine. Through the years, different investigations and reports have been carried out regarding this problem. However, considering that the mine concession over the years has passed to different operators, whose goals and targets also changed, the studies and reports do not share the same approach.

As part of this study, a compilation of various reports and studies conducted in the Asse mine II concerning fluid inflow into the mine was conducted (Fig. 1.2). This chapter provides a summary of the results and conclusions from these reports regarding the historical record of fluid ingress into the mine, its potential flow pathways, geological and geochemical analyzes, and the outcomes of previous geophysical explorations.

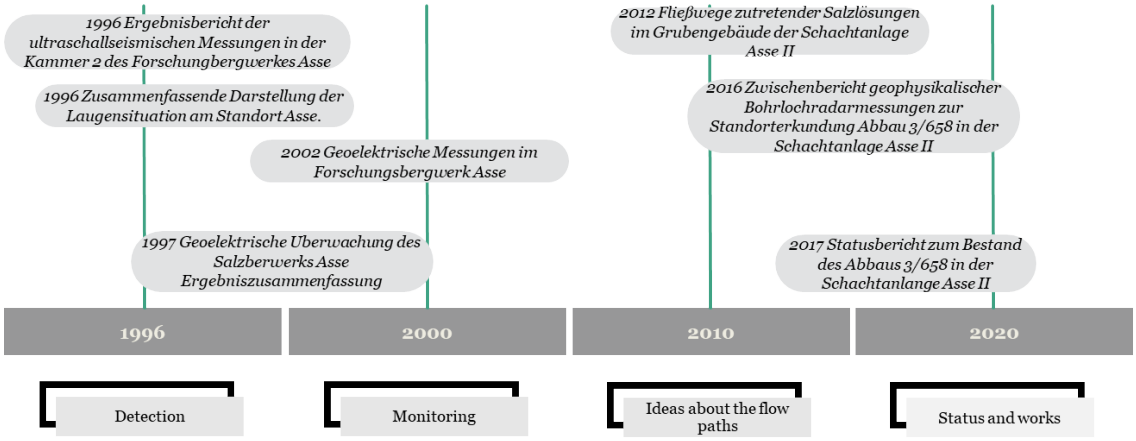

Figure 1.2: *Timeline of fluids inflow related reports.*

1.1.1 Historical reports of fluid inflow points and their movement over time

The mine has undergone three main phases: mining phase (1909-1964), open maintenance phase (1965-1994), and displacement phase in the southern flank (1995-2004).

In August 1988, the first dripping point was discovered on the southern flank of the Asse II mine (GSF, 1996). This one appeared on the roof of chamber 5 at level 553 m. Since then, different reports have recorded the fluid entry points into the mine and their migration over time.

Below is a summary of the historical events reported in GSF (1996):

- In August 1988, a drip point was detected on the southern flank, in former rock salt, on the roof of chamber 5 level 553 m, and afterwards in six other locations.
- At the end of August 1988, a drip point was detected at level 532 m. The operator tried to collect the inflow of solutions, but parts ran past the detection system.
- In January 1989, previous undetected solutions showed up on levels 616 m and 637 m, also in chamber 5. These points had all been dried up, but at different times. This difference in drying times could be attributed to certain paths receiving fluids for longer durations than others. Additionally, the force of gravity caused a time delay of over three months.
- In April 1989 at level 658 m, in chamber 3 (approx. 100 m west of chamber 5) an old dried-up drip location became active.
- In September 1989, when the upper drip point in chamber 5 was already dry, a new dripping point was discovered at level 574 m in chamber 3. This was active during nine months.
- In March 1991 a new dripping point was discovered at level 637 m in chamber 3. Over time, this point has evolved into the most active inflow point. The inflow quantities were increasing therefore in August, a drainage bore was drilled from level 658 m through chamber 3 at level 637 m. Since then the inflow rate have steadily increased to higher values an at the end of April 1995 it was about 8 m^3/day.
- In March 1992, the drip point at 574 m finally dried up.
- Level 658 m was only active when the acquisition of the solution in level 637 m was incomplete. The same occurred with levels 700 m and 750 m.
- In 1994, a section of chamber 3 at the 637 m level collapsed, causing damage to the fluid collection system. Consequently, some of the fluids migrated to lower levels.

Linder and Thoma (1996) report that in the time when their measurements took place, in level 637 m, the inflow in chamber 3 entered at a rate of 9 m^3/day. It was no longer accessible. Chamber 4 was already filled and chamber 2 was partially filled.

Between 1991 and 1996, the inflow solution in chamber 3 was collected using a plastic film placed in the southern mining area of chamber 3 level 637 m. The solution was then directed to the 658 m level through a borehole (L658020) and collected in storage containers. Approximately 9 m^3/day of solution was collected using this method in 1994 (Brauer, 2017).

In 1996/97, a sealing measure was carried out in chamber 3 level 658 m. This measure included the installation of a large-scale plastic sealing membrane (depository film) and drainage pipes to collect and drain the solution released in the mining chambers (Brauer, 2017). After the installation of the collection system, the amount of solution collected in the southern flank of the 658 m level increased gradually from 1998 to December 2001, reaching a collection rate of approximately 11 m^3/day. The collection rate further increased to around 12 m^3/day between January 2001 and January 2002. There were fluctuations in the collection rate over the years, with repairs and maintenance affecting the rate. The overall collection rate in the southern flank of the mining field stabilized at around 12.5 m^3/day by December 2014 (Brauer, 2017).

Geotechnical measurements done through the years in chamber 3 level 658 m and summarized in Brauer (2017) confirm high levels of mechanical stress and deformation, particularly in the vicinity of the excavation. The ongoing deformations at the west side of the mine are likely to further impair the functioning of the drainage system and increase the migration of solutions to lower levels. The chemical composition of the solutions, combined with the presence of potassium salt formations, could have a detrimental effect on the surrounding areas.

As stabilization and prevention measures, the mine chambers have been back-filled with various materials over the years. Wolff (2021) indicates that at Asse II, 3,881,000 m^3 of salt, 407,200 m^3 of Sorel concrete, and 12,280 m^3 of gravel have been introduced. Following the completion of these stabilization and prevention measures, it is expected that approximately 110,900 m^3 of empty space will remain open.

Naumann and Rölke Christopher (2019) present a characterization of back-filling samples from chamber 3 in level 658 m. This laboratory program focused in particular on determining the strength of the backfill and its permeability on three varieties of rock salt back-fill presented in the chamber. The permeability tests carried out on this material resulted in determined gas permeabilities in the range of $k = 10^{-15}$ to 10^{-16} m^2.

1.1.2 Flow paths

Gärtner (2012) provides an analysis of the flow paths of salt solutions in the mine structure of the Asse II facility.

The deformation in the southern flank of the Asse II mine caused by mining activities has led to the opening of flow paths for salt solutions. This occurs where the bending of the rock layers above the mining area and the stress distribution in the rock mass create a mechanical stress situation. The combination of strain in the direction of the Asse anticline and the weakening of separation surfaces in the transverse direction leads to the opening of naturally occurring structures. As a result of ongoing rock mechanical reactions, the salt solution penetrates deeper into the loosened zone of the southern flank.

The potential migration pathway is assumed to be through finely fractured anhydrite rock.

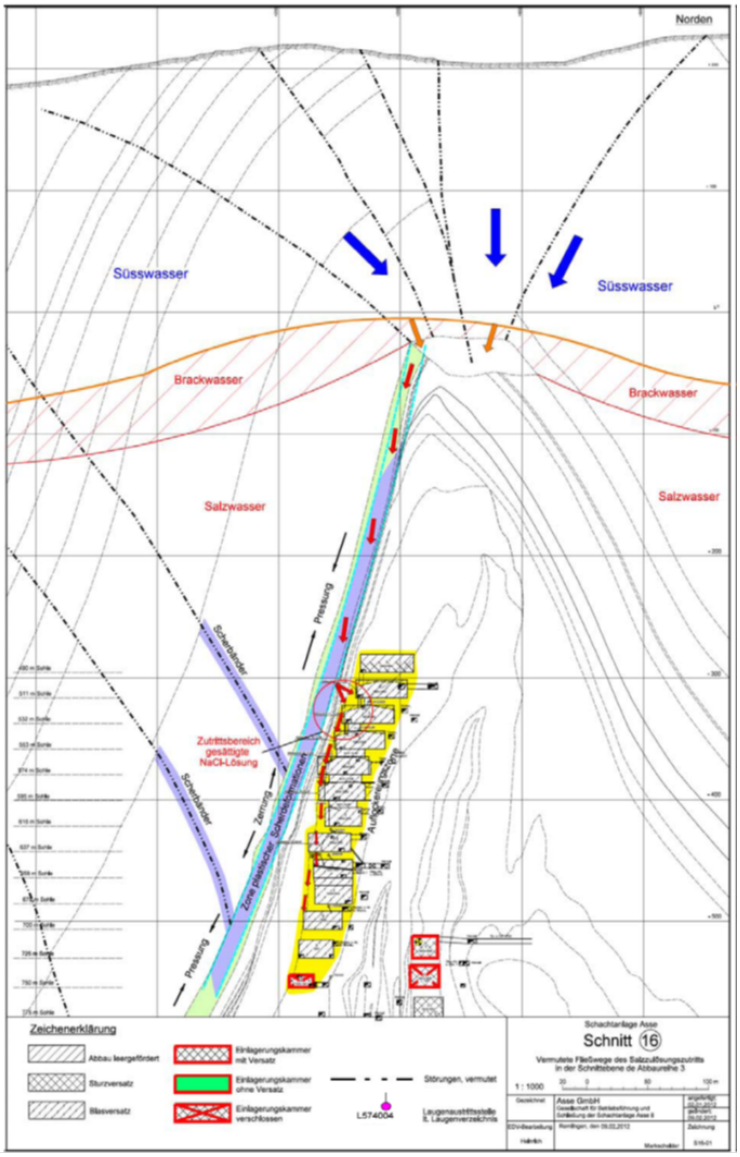

Figure 1.3: *Schematic representation of the flow paths of the fluids in the area of chamber 3 (Gärtner, 2012).*

This migration occurs in the loosened area behind the southern edge of the excavations, extending a few meters (Gärtner, 2012).

The migration path between the overlying rock and the salt rock is assumed to be between depths of 500 and 574 meters. The first outflow point into the mine chambers was discovered in 1988 in chamber 5 on the 532 m level. The outflow point in chamber 3 was located on the level 574 m in 1989. Over time, this outflow has migrated to deeper levels in the southern boundary of the mining panels or their hanging walls (Fig. 1.3). The exact path of the salt solution into the mine chambers is not known, and there are different ideas about its migration within the southern boundary of the mine chambers (Gärtner, 2012).

1.1.3 Geochemistry analyzes

GSF (1996) presents a summary of the results of different chemical analyzes carried out up to 1996. Among these results are the following findings and conclusions:

The in-flowing solutions are mixed solutions of two components. One component comes

from the overburden, the other has its origin in the salt formation itself. The overburden component consists of a NaCl and $CaSO_4$ saturated solution with a relatively high proportion of $CaCl_2$. Such solutions were detected in the deep boreholes R5 and R7 in the lower Muschelkalk. They were saturated with halite, anhydrite and carbonates and were formed by the dissolution of shell limestone and reactions with carbonate rocks.

The second component from the interior of the salt formation was formed by the dissolution of carnallite (K_2C). This solution is rich in $MgCl_2$ and $MgSO_4$ and saturated in halite, carnallite, and kainite. In the quinary system of the salts of oceanic salt deposits, the composition of this solution lies between Q and R, accordingly, it is indeed saturated with halite, carnallite and kainite, but not with sylvin and not yet fully saturated with kieserite (GSF, 1996).

Mixing the two components creates solutions containing NaCl and $MgCl_2$, which contain $CaCl_2$ or $MgSO_4$, depending on the mixing ratio. Irrespective of the mixing ratio, the mixed solutions are always saturated with halite.

Initially, according with the results in GSF (1996), the migration of the overburden solutions from their storage area, through the lower Muschelkalk, and the upper Buntsandstein, into the salt dome and the mine chambers possibly takes place along a fault zone. Geological evidence from boreholes R1 and R6, along with geophysical measurements, suggested the presence of such faulty rock. The mixing of the two components in the solution likely happens before they enter the chambers, possibly within a stress system caused by rock mechanics. The summary of all chemical findings and the results of the geochemical model calculations in GSF (1996) allow the conclusion that the inflow on the southern Asse flank could be an open reservoir with free paths to the overburden.

The inflow quantities into the mine do not depend on the changing chemistry but are determined by the existing paths and the existing hydraulic gradients. Since all solutions, including the overburden component, are saturated with halite, an increase in the paths through dissolution is not to be expected. It cannot currently be ruled out that the inflow process is also influenced by the deformation processes on the southern flank of the Asse anticline. However, since there is insufficient data on the reservoir, prevailing hydraulic gradients, transmissivities, and fracture permeabilities, no sufficiently reliable statement can be made on the hydraulic processes.

Later Gärtner (2012), summarizes the types of solutions present on the southern flank of the Asse mine II, describing a total of five types of solutions:

Residual solutions in the Asse II mine are saline solutions stored within the evaporite rocks. They are typically saturated with multiple components such as NaCl and KCl. These solutions have higher salt content compared to groundwater stored in the surrounding rocks.

Metamorphosis solutions are solutions that result from the transformation of compounds crystallized from seawater. The chemical composition of these solutions depends on the specific evaporite rock involved in the metamorphosis.

Back-filling solutions are solutions that result from the extraction of potash salts. The residues from the processing of raw salts, including halite, anhydrite, clay minerals, and other compounds, are mixed with solution remnants and reintroduced into the mine chambers. These solutions are generally limited in quantity and contain up to 20% water.

Operating solutions refer to anthropogenic solutions encountered in the mine for technical reasons, such as wash water and flushing water. Their chemical composition can vary depending on the source and possible contact with evaporite rocks or residues.

Overburden solutions originate from an open system and have connections with groundwater-bearing layers in the surrounding rocks (are connected to groundwater-bearing layers in the overburden). These solutions have lower densities, typically around 1.2 g/cm^3, and contain low levels of rubidium (Rb) and bromine (Br). They have been observed to seep into mine workings in the salt mining area of the southern flank, causing mechanical effects on the stability of the salt rock.

The main collection point for the salt solutions from the overburden is in chamber 3 on the 658 m level. On the way to deeper areas, the solution changes its chemical composition. This can be caused by:

1. Evaporation

2. Reaction with adjacent rock (rock salt, carnallite)

3. Reaction with backfill (Ronnenberg, old backfill)

4. Reaction with introduced building materials (calcium silicate brick, mortar, Sorel concrete)

Based on their composition (e.g., trace elements or NaCl content), the chemically modified solutions can be assigned to the overburden solution that emerges from chamber 3 level 658 m (Gärtner, 2012).

1.1.4 Geophysical studies

Different geophysical studies have been carried out over the years at the Asse mine. Some of these studies aimed to obtain a better understanding of the fluid inflow situation and its monitoring.

In November 1995 a geoelectrical tomography was done (section east-west) in chamber 3 level 637 m. On this tomography it could be observed that the western part of the southern flank was the wettest, the eastern part less, and in the middle, there was a slightly drier area. However, it should be noted that dry salt rock has resistivities of the order of 10^{-5} to 10^{-6} Ω/m (GSF, 1996).

Linder and Thoma (1996) present the results of the ultrasonic seismic measurements that took place on the southern flank of the Asse mine at level 637 m. Chambers above and below level 637 m were no longer accessible at that time. Therefore, the study was made only in chamber 2, and the cut-through chamber 3. The aim of this study was to explore the structures present (in connection with small tectonic elements), using the ultrasonic seismic reflection principle in the frequency range 20 - 50 kHz, which detected fractures widths of less than 1 mm (25 kHz) up to 0.05 mm (50 kHz) and gave a depth penetration of approximately 180 m towards the SW direction of the chamber. The ultrasonic seismic investigation was carried out at four different elevation levels. As result, the geological interpretation of the four measurements and their subsequent interpolation was obtained. Parallel stratification to the southern side of chamber 2 could be observed, but some dislocations were found. The displacements within bed boundaries are between 3 and 8 m. Small, isolated migration paths (cracks) in the millimeter range, were identified and could also be linked to locally limited tectonic faults. This fracture goes as far as Rötten soT1. Nevertheless, it could not be ruled out that these microcracks or even fine hairline cracks will expand preferentially under geomechanical stress.

In 1997 a geoelectric monitoring using a Wenner arrangement was made at levels 490 m, 616 m, 637 m, 658 m, 700 m, and 750 m (Hente, 1997). As part of the results, the specific resistances were determined to correspond to those of dry rock salt at most measuring

points. The lower values determined in part at the 490 m level were still above those expected for sandstone. It is possible that the anomalies were slightly loosened zones in the anhydrite, which is otherwise also very poorly conductive. As a general conclusion, the moisture was limited to only a number of small crack surfaces.

The geoelectrical monitoring continued, and Hente (2002) presents the geoelectrical monitoring study which was made at 4 to 8 different times and the result was compared over time as well as in different levels (616, 490 m, 637 m, 700 m, 750 m). From these tomographies, it could be seen how the moisture in the different chambers varied over the years.

Reflection and cross-hole measurements were carried out with various borehole radar probes in slightly inclined boreholes on November 2015, located in chamber 3 level 658 m in the Asse II facility. These measurements aimed to assess the condition of the surrounding rock mass and pillars, detect potential foreign objects, and provide information on the moisture content of the back-fill. The results of the reflection measurements in the first phase confirmed the presence of heterogeneities in the pillar between the spiral access route and chamber 3 level 658 m. Additional reflectors were identified in the area, indicating potential structural variations (Lehmann, 2016). The cross-hole measurements in the second phase verified and complemented the results of the reflection measurements. The graphs and attenuation curves showed variations in signal amplitude and velocity, indicating potential areas of increased moisture content and the presence of linear and air-filled structures in the displacement (Lehmann, 2016). This study revealed that the moisture content increases towards the western and upper southern areas of chamber 3/658 m. The identified trends suggest that the moisture content may be even higher in deeper areas of the excavation (Lehmann, 2016).

1.2 Field data

As mentioned before, the mine faces fluid inflow and instability, threatening the integrity of the stored nuclear waste. For safety reasons, nuclear waste retrieval is imperative, demanding detailed structural insights to construct a new shaft. In the pursuit of imaging the salt dome structure in the Asse area, a groundbreaking 3D seismic survey was conducted, utilizing innovative approaches and cutting-edge technology. The seismic acquisition methodology employed a dense grid of over 41,000 nodes (geophones), showcasing the resilience of nodal seismic acquisition in challenging terrains. This acquisition took place between October 2019 and March 2020, and it covered 37.5 km^2, incorporating urban areas, and forest. The survey achieved an impressive 93% coverage of the originally planned area, showcasing the efficiency of the seismic nodal system (Trela et al., 2021).

This chapter delves into the field data acquisition, including its parameters, data quality, and its pre-processing.

1.2.1 Field data acquisition:

The acquisition involved a regular geometry with orthogonal source-receiver lines to map steep formations at depths of around 2000 m. Long offsets and wide-azimuth distribution were crucial, with variable spacing to enhance resolution in specific areas (Fig. 1.4). The mobile data processing center, designed for high efficiency and zero-error tolerance, played an important role. A computational power test favored graphics processing units (GPU), demonstrating 6.5 times higher performance than CPU equivalents. The survey achieved a remarkable daily productivity of around 1000 shot points in a mixed-source project, necessitating meticulous planning and logistics management (Trela et al., 2021).

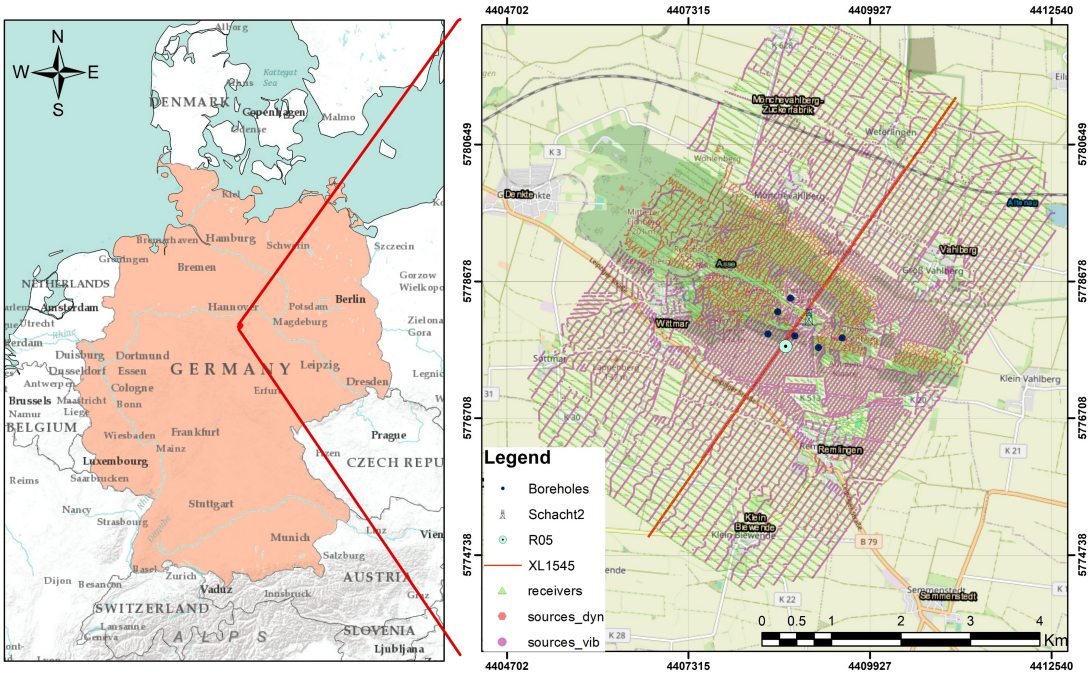

Figure 1.4: *Location of the survey area.*

The acquisition parameters, shown in Table 1.1, highlight the details of the survey setup. Source line spacing, point spacing, sweep characteristics, and receiver line spacing were adjusted to meet the challenges of the diverse terrain. The inclusion of a wireless nodal system with 44,677 nodes equipped with 5 Hz geophones underscored the adaptability of the technology, allowing for efficient data collection.

Two kinds of sources were used in this acquisition. In agricultural and urban areas, a slip-sweep technique utilized vibrators, while the challenging terrain prompted the replacement of Vibroseis sources with dynamite in certain regions (Trela et al., 2021). This combination, accounting for approximately 18% of total sources, necessitated specific considerations due to potential influences on modeling and full Waveform Inversion (FWI).

Table 1.1: *Basic acquisition parameters. Modified from Trela et al. (2021)*

Source line spacing	Variable (50 m, 100 m, 200 m)
Receiver line spacing	Variable (50 m, 100 m)
Source point spacing	10 m
Receivers point spacing	10 m
Number of active channels	41, 190
Source type	Vibrators and dynamite
Number of vibrators	4 – 5 in slip-sweep technique
Sweep frequency range	5 – 120 Hz
Sweep length	60 s
Sweeps	1
Final trace length	4 s
Sampling interval	1 ms
Recording system	Internal 5 Hz geophone

Standard quality control (QC) procedures were adapted to seismic measurements, facing challenges due to the requirement to register all shot points with full spread. Final data

quality control and positioning verification occurred after collecting all sensors, employing innovative approaches to address the large volume of recorded traces.

1.3 Overview and objectives

The infiltration of fluids into the Asse mine poses a significant threat, potentially leading to instability within the salt shield. Moreover, recent processing of dense 3D seismic data has revealed imaging anomalies on the south flank of the Asse structure, possibly linked to fluid presence. This study aims to investigate the seismic signatures of fluid pathways within the host rocks on the basis of the recently acquired dense seismic data.

Building upon previous reports and discussions with the BGE geophysics and geology team, the prevailing hypothesis suggests that fluid migration towards the Asse mine on the southern flank of the anticline structure may occur through the Röt-1 Anhydrite B unit of the Upper Buntsandstein group. This unit is estimated to have a thickness of approximately 14 to 18 m. Given the fluids pathway hypothesis in the Asse structure, the topic of whether we can find direct or indirect seismic signatures has been posed.

This study has the objective of providing insights into the seismic response to fluid pathways, which could contribute to the interpretation of seismic data from the Asse II mine:

- Analyze the seismic response to different properties and configurations (e.g., wave propagation velocities, density, thickness) of the Röt Anhydrite B formation.
- Identify changes in reflection coefficients, tuning effects, and scattering resulting from alterations in the Röt Anhydrite B layer.

1.3.1 Thesis outline

To address these objectives, a comprehensive methodology combining 2D forward modeling and field data analysis were employed. The thesis structure starts with an introduction providing an overview of the research problem, objectives, and methodology, follow by a theoretical background (Chapter 2) which covers essential theory relevant to seismic data analysis, fluid in seismic data, and seismic signatures. The geological background (Chapter 3) offers detailed information about the geological context of the Asse II mine.

The study's data processing and findings, which is split into three sections, follow afterwards:

1) Forward modeling a 2D section of the Asse structure in order to determine where on the surface we might anticipate signatures from the dipping reflector (Chapter 4); this section covers the setup and outcome of the forward modeling.

2) Thorough examination of the Röt Anhydrite B formation interfaces: in Chapter 5, the configuration and outcomes of various tests are shown in a more simplified model to investigate the specific seismic responses of reflection coefficient tuning and scatering effects in the Röt Anhydrite B layer when its parameters are altered.

3) Analyzing the field data at various dip angles and frequencies (Chapter 6).

Chapter 2

Theoretical background

This section introduces the theoretical frameworks, and concepts that lay the groundwork for the subsequent discussion in the following chapters.

2.1 Wave propagation

A seismic wave is an impulse of elastic strain energy that propagates outwards from a seismic source. There are two types of seismic waves: surface waves and body waves.

Body waves are energy waves that propagate through the Earth's interior in response to seismic sources. Most of the energy propagates as primary waves (P-waves) and secondary waves (S-waves). P-waves are the fastest and are compressional waves, causing particles to move back and forth parallel to the direction of wave propagation. S-waves, on the other hand, are shear waves, and they can only propagate through solids and not through liquids or gases. Shear waves cause particles to move perpendicular to the direction of wave propagation (Fanchi, 2010).

P-wave velocity (v_p) depends on the elastic properties and density of the medium, and the velocity of S-wave (v_s) depends on the shear modulus and density of the medium:

$$v_p = \sqrt{\frac{K + 4/3\mu}{\rho}}, \tag{2.1}$$

with bulk modulus K, shear modulus μ, and density ρ. The propagation of v_s is given by

$$v_s = \sqrt{\frac{\mu}{\rho}}. \tag{2.2}$$

Seismic wave propagation can be explained as the transmission of energy through an elastic medium. The wave equation describes how waves propagate through a medium. In other words, it describes how waves travel through the Earth's subsurface, interacting with various geological materials and structures. The wave equation for an elastic, homogeneous medium, is as follows:

$$\rho \frac{\partial^2 \boldsymbol{u}}{\partial t^2} = (\lambda + 2\mu)\nabla(\nabla \cdot \boldsymbol{u}) - \mu \nabla \times (\nabla \times \boldsymbol{u}), \tag{2.3}$$

Whereρ is the mass density of the medium, λ and μ are Lame's constants and u is the displacement of a medium particle from its undisturbed state (Fanchi, 2010).

Seismic response is measured by the reflection generated at an interface according to the properties of the layers above and below the boundary and the nature of the seismic pulse impinging on that boundary (Herron, 2011). This response is characterized by changes in the amplitude, frequency, phase, and polarization of seismic waves as they move through the Earth's subsurface and interact with various geological features through reflection, refraction, scattering, and attenuation. By analyzing the seismic response, it is possible to infer information about the subsurface structure, including the presence of oil, fluids or variation in the composition of the rocks (Tucker and Yorston, 1973).

A seismic signature is essentially the unique set of seismic data characteristics that relate to the geological structures and materials through which seismic waves have travelled. It reflects a combination of factors such as lithology, rock texture, porosity, pore shape, pore fluid types, degree of compaction, temperature, and subsurface anisotropy. These factors influence the elastic properties of seismic waves, specifically P-wave velocity, S-wave velocity, and bulk density, creating a distinctive pattern on seismic recordings that can be used to infer the subsurface characteristics, including the presence of fluids (Fawad et al., 2020).

Seismic traces correspond to the recorded signals of seismic waves that have propagated through the subsurface and returned to the surface. They can be represented as the result of convolving a seismic signal with a series of reflection coefficients. Seismic reflection traces provide crucial seismic attributes like amplitude, phase, polarity, and arrival time, aiding in geological interpretation. Polarity information is vital for calibration with well data and identifying lithologies. Reflection polarity is particularly important for confirming high-amplitude anomalies, crucial in fluids detection. The waveform and arrival time of reflections depend on rock properties and depth, carrying significant geological information encoded in the seismic attributes (Nanda, 2021).

2.2 Seismic reflection and refraction

The impedance is used to measure the contrast between two adjacent layers in the subsurface; it is described as the product of density and velocity. When a seismic wave meets a chance in acoustic impedances (I) it is partially transmitted and partially reflected, and the reflected wave can be detected at the surface. The acoustic impedance changes when there is a variation in either density (ρ_B) or compressional velocity (v_p) as the wave propagates between different mediums.

$$I = \rho v_p. \tag{2.4}$$

The seismic reflection coefficient (RC) depends on the acoustic impedances in two adjacent layers. The reflection and transmission (TC) coefficient, respectively, when the incident plane wave is propagating in a direction that is perpendicular to a horizontal reflecting interface are given by

$$RC = \frac{I_2 - I_1}{I_2 + I_1}, \tag{2.5}$$

$$TC = \frac{2I_1}{I_2 + I_1}, \tag{2.6}$$

with I_1 and I_2 are the acoustic impedances of the two layers.

The reflection coefficient at an interface relies on the contrast in acoustic impedance for normal incidence. In practical seismic data acquisition, there is typically a distance between the source and receiver (offset), therefore the waves arrive at the interface at different angles of incident. This implies the reflection becomes more complicate, as a portion of the P-wave energy will transform into both reflected and transmitted S-waves (Bacon et al., 2013).

Snell's law expresses the relationship between the angle of incident of the wave and transmission for a plane interface. When a wave crosses a boundary between two isotropic media, the wave changes direction such that the ratio of the sines of angle of incidence (θ_1) and angle of refraction (θ_2) is equal to the ratio of the velocities (v_1/v_2) in the two media. A critical angle exists if the velocity increases with depth across the interface.

$$\frac{\sin\theta_2}{v_2} = \frac{\sin\theta_1}{v_1}. \tag{2.7}$$

Zoeppritz (1919) derived equations describing how the amplitudes of reflected and transmitted P- and S-waves depend on incidence angle and medium properties. These amplitudes are influenced by the contrast in Poisson's ratio (ν) and impedance across the interface (Bacon et al., 2013). The result is a complicated set of equations, the Zoeppritz equations. They allow the calculation of all reflection and transmission coefficients for P- and S-waves.

$$\begin{bmatrix} -\sin\theta_1 & -\cos\varphi_1 & \sin\theta_2 & -\cos\varphi_2 \\ \cos\theta_1 & -\sin\varphi_1 & \cos\theta_2 & \sin\varphi_2 \\ \sin 2\theta_1 & \frac{V_{P1}}{V_{S1}}\cos 2\varphi_1 & \frac{\rho_2 V_{S2}^2 V_{P1}}{\rho_1 V_{S1}^2 V_{P2}}\sin 2\theta_2 & \frac{-\rho_2 V_{S2} V_{P1}}{\rho_1 V_{S1}^2}\cos 2\varphi_2 \\ -\cos 2\varphi_1 & \frac{V_{S1}}{V_{P1}}\sin 2\varphi_1 & \frac{\rho_2 V_{P2}}{\rho_1 V_{P1}}\cos 2\varphi_2 & \frac{\rho_2 V_{S2}}{\rho_1 V_{P1}}\sin 2\varphi_2 \end{bmatrix} \begin{bmatrix} R_{PP} \\ R_{PS} \\ T_{PP} \\ T_{PS} \end{bmatrix} = \begin{bmatrix} \sin\theta_1 \\ \cos\theta_1 \\ \sin 2\theta_1 \\ \cos 2\varphi_1 \end{bmatrix} \tag{2.8}$$

The Zoeppritz equations provide a precise description of the amplitude distribution occurring at the interface between two elastic isotropic half-spaces. Nevertheless, these equations are difficult to implement to determine amplitude variation with angle due to their complicate algebraic expressions (Ge et al., 2022).

When plotting the reflection and transmission coefficients against the angle of incidence, it helps to understand how much of the incident wave is reflected back and how much is transmitted into the next layer. The plots illustrate how the amplitude of the reflected and transmitted waves change with varying angles of incidence. This information helps to interpret seismic data and to infer the properties of subsurface layers, such as changes in rock properties. Furthermore, it is possible to observe the critical angle, where at this angle the reflection coefficient reaches 100%. At angles greater than the critical angle, the refracted wave cannot propagate into the second medium and is instead completely internally reflected (Castagna and Backus Milo M., 1993).

Factors influencing seismic wave propagation

Seismic waves traveling through the Earth encounter various discontinuities between different rock types, resulting in phenomena like reflections, diffractions, absorptions, scatterings, and transmissions (refractions). Absorption causes energy loss due to conversion of mechanical energy to heat through friction at grain contacts, cracks, and fluid-filled pores in rocks. Absorption is frequency selective, resulting in reduced energy with lower frequency and amplitude at deeper depths. Scattering losses result from irregular dispersions of energy due to heterogeneity in rock sections, often appearing as apparent noise in seismic

records. Transmission is a loss of energy as the wave encounters lithologic boundaries, with part of the energy reflected back to the surface and less transmitted deeper into the Earth. Transmission losses reduce amplitudes at all frequencies and are not frequency selective like absorption. And Spherical (Geometrical) Divergence corresponds to energy reduction as the seismic wave spreads through the subsurface in a spherical wavefront, leading to attenuation with distance from the source. This decay is dependent on the distance traveled and increases with higher velocities (Nanda, 2021).

The intrinsic seismic properties such as amplitude and velocity are influenced by the properties of the rocks through which the wave travels. The elasticity and density of rocks primarily determine seismic amplitude and velocity, though porosity, texture, fractures, fluid saturation, viscosity, and factors such as pressure and temperature also affect the seismic properties (Nanda, 2021).

The seismic response varies with different offsets or angles of incidence due to several factors related to the properties of the subsurface layers and the geometry of seismic wave propagation. Between this factor is Angle-Dependent Reflectivity. Additionally, at different offsets, there might be changes in the relative strength and timing of ghosts and multiples, which can affect the seismic response (Herron, 2011).

Variation in the amplitude in seismic data provide valuable information about subsurface features such as lithology, fluid content, and structural heterogeneities. However, interpreting seismic amplitudes requires consideration of various factors that can influence their magnitude and distribution (Sheriff, 1975). Some of the factors affecting amplitudes in seismic data and their implications for geological interpretation are geological factors, including lithology, fluid content, and porosity, that have a significant influence on seismic reflection amplitudes, with porous reservoir rocks typically displaying strong negative amplitude anomalies due to low impedance contrasts at fluid interfaces. Acquisition and processing factors, such as offset distance and receiver configuration, also impact recorded amplitudes, alongside source characteristics and data processing techniques. Subsurface conditions, encompassing velocity variations, structural heterogeneities, and anisotropy, further contribute to amplitude distribution complexities. In adition, environmental factors, like surface conditions, introduce additional complexities. Accurate seismic interpretation necessitates a comprehensive understanding of these interrelated factors, facilitating precise subsurface characterization crucial for geological and reservoir modeling endeavors (Denham, 1984).

Fluids effects

The presence of fluids within rock formations can significantly affect their seismic response, and this has been widely studied mainly in the hydrocarbon sector. Different fluids, such as oil, gas, and brine, change the rock properties in ways that can be detected on seismic surveys (Bacon et al., 2013; Nanda, 2021). The effects of fluids include:

Velocity Changes: When gas (air) replaces brine in the pore spaces, the P-wave (compressional wave) velocity decreases significantly compared to the brine case. Gas has a developed effect even at a few percent saturations.

Density Reduction: Gas saturation increases lead to a decrease in rock density, which happens almost linearly as the gas saturation increases.

Impedance Contrast: Because of the combined effect of velocity decrease and density decrease, the acoustic impedance (product of rock density and seismic velocity) of gas-saturated rocks drops sharply from the brine case and then decreases gradually with increasing gas saturation.

Attenuation Effects: Fluids alter the attenuation characteristics of seismic waves, having implications on both the amplitude and frequency content of the seismic signals.

S-wave Velocity: Fluids have a minor effect on S-wave (shear wave) velocity; for the oil and gas cases, the S-wave velocity is slightly higher due to the effect on density.

Amplitude Variation with Offset (AVO): The presence of fluids can cause a recognizable AVO effect. This occurs because the seismic wave's amplitude changes with different angles or distances from the source, often indicating the type of fluid within the geological structure.

The theory of poroelasticity is a widely used petrophysical modeling approach to predict the velocities of P-waves in fluid-saturated porous rocks when seismic waves pass through them. This theory was first introduced by Biot in 1941 and later expanded upon by Gassmann (1951). Gassmann's equations are commonly used to calculate the effect of fluid saturation on seismic properties, although they have limitations, especially in heterogeneous reservoirs (Nanda, 2021). Rock matrix and fluid characteristics both affect seismic qualities and given the reality of wide variations that commonly occur in nature, it might not always be simple to distinguish one from the other (Nanda, 2021).

Tuning effect

The tuning effect in seismic data is a phenomenon characterized by the amplification or curtailment of reflection amplitudes as the thickness of thin beds approaches certain multiples of the seismic wavelength (Nanda, 2021). A comprehensive understanding of these effects is essential for precise interpretation and analysis in seismic exploration. This is due to the fact that tuning effects can obscure or highlight reservoir characteristics, making it challenging to accurately assess reservoir properties, such as thickness or fluid content (Simm and Bacon, 2014).

Some effects of tuning in seismic data are:

Amplitude modification, amplitude enhancement: The phenomenon of constructive interference arises when the thickness of a geological layer is approximately a quarter-wavelength, resulting in a substantial increase in amplitude. Amplitude diminishment: Conversely, as the thickness of the layer approaches a half-wavelength, destructive interference occurs, leading to a reduction in amplitude (Naseer and Asim, 2018). Below 1/4 of the wavelength, the thin beds cannot be detected. In practical terms, tuning thickness serves as a useful gauge for vertical resolution (Simm and Bacon, 2014; Nanda, 2021; Saeed et al., 2020).

Frequency dependency: Tuning effects are frequency-dependent. different frequencies exhibit varied tuning responses, impacting the seismic reflection amplitudes.

In zero-phase seismic data, tuning effect happens when the peak of a positive reflection aligns with the peak of the negative reflection's side lobe, leading to a notably brighter amplitude.

The typical methods employed to examine primary attributes for thin beds properties involve the tuning thickness. The tuning thickness is determined by using the following equation (Nanda, 2021):

$$z = \frac{v_1}{4f} \tag{2.9}$$

where z is the tuning thickness of a bed, usually ¼ of the wavelength ($\lambda/4$), v_1 is the interval velocity of the target layer, and f is the dominant frequency. However, precise

thickness estimation of thin beds requires separate processing techniques like trace analysis and spectral decomposition (Nanda, 2021).

2.3 Seismic modeling with finite differences

Seismic modeling is often used to better understand the observed seismic response to geologic changes and to assertively assign these variations to the properties of rock and fluid (Nanda, 2021). Different techniques, including wavenumber integration, ray-tracing, finite elements, and finite differences, have been developed for seismic wave modeling in complex media.

The finite-differences (FD) method is employed to numerically estimate wave propagation in complex models, where analytical solutions are impractical. This method involves approximating spatial and temporal derivatives in the wave equations using FD operators, facilitating computational efficiency and implementation. Bohlen (2002) originally developed the seismic forward modeling program SOFI2D, which is based on a 2D finite-difference approach in the time domain (e.g., (Tarantola, 1984; Crase et al., 1990; Gauthier et al., 1986).

The algorithm employs dynamic variables and material parameters distributed across staggered spatial locations on a cubic finite difference cell. The dynamic variables describe wave propagation, while material parameters define the structure and properties of the viscoelastic medium. Stability and numerical dispersion are crucial considerations in finite difference modeling, ensuring accuracy and realism in complex models (Bohlen, 2002).

Grid dispersion is a critical aspect to consider in forward modeling using finite difference methods. It ensures accurate representation of wavefields within the computational grid. In SOFI2D, the grid dispersion is assessed to determine the optimal spatial grid point distance (Δh) required for faithful sampling of the wavefield. It needs to ensure that the space between grid points has to be satisfied:

$$\Delta h \leq \frac{\lambda_{\min}}{n} = \frac{v_{\min}}{n f_{\max}}. \tag{2.10}$$

The stability of the simulation is also assessed, focusing on temporal discretization. it ensures that the time step (Δt) satisfied the Courant-Friedrichs-Lewy criterion, which dictates that Δt should satisfy:

$$\Delta t \leq \frac{\Delta h}{h\sqrt{2} v_{\max}}, \tag{2.11}$$

where $v_{\max}$ is the maximum velocity in the model. The factor h depends on the order of the FD operator.

Chapter 3

Geological context of the Asse salt structure

3.1 Geological evolution

The geological evolution of the Subhercynian Basin, situated in northern Germany, spans a significant timescale, encompassing diverse geological processes and formations over millions of years.

The basin's origins trace back to the Paleozoic Era, approximately 540 million years ago. During this time, the region experienced the deposition of sediments, including sandstones, shales, and conglomerates, forming the initial layers of the basin. These deposits delineate an environment indicative of shallow marine settings characterized by fluctuating sea levels and rich marine biodiversity (Scheck et al., 2003).

Throughout the Mesozoic Era, the region experienced notable tectonic activity due to the fragmentation of the supercontinent Pangaea. Rifting and the separation of landmasses caused subsidence in some areas, including the Subhercynian Basin. This period marked continued sedimentary accumulation, incorporating layers of sandstones, clays, and limestones.

These sediments preserved a record of changing environments, including marine transgressions and regressions, as well as the presence of fossils indicating past life forms.

As the Cenozoic Era dawned, the region experienced uplift and erosion, altering the landscape. The basin underwent modifications due to the movements of Earth's crust, which influenced its shape and structure. Terrestrial environments dominated, with the presence of vegetation and the accumulation of organic material that later formed lignite deposits (Scheck et al., 2003; Scheck-Wenderoth and Lamarche, 2005).

During the Pleistocene epoch, the area was affected by glacial advances and retreats. Ice sheets covered the landscape, shaping the terrain through erosion, and leaving behind glacial deposits as till, moraines, and outwash plains that contributed to the region's geological diversity (BGE, 2018; Szymaniak and Schäfer, 2002).

3.2 Stratigraphy

Units from the Paleozoic to the Cenozoic are found in the research region. Due to the Subhercynian Basin's southern boundary, there are certain facial deviations between the Lower Saxony Basin's normal sequence and the usual stratigraphic sequence. The

generalized stratigraphic column of the Mesozoic sequence in the Asse-Heeseberg mountain range is displayed in Fig. 3.1. It's worth noting that in the Asse anticlinal structure, the sequence is not normal, with the Zechstein unit in contact with the Upper Buntsandstein (so) on the southern flank and with the Lower Buntsandstein (su) on the northern flank of the anticline.

The region's geological unit description is presented next.

3.2.1 Perm

Zechstein (z)

This unit consists of deposits of carbonate and sulfate rocks with mudstones, evaporites, and carbonates. Zechstein is the oldest mapping unit in the area, it is not possible to determine its thickness (Szymaniak and Schäfer, 2002).

3.2.2 Triassic

Lower Buntsandstein (su)

The Lower Buntsandstein according to Szymaniak and Schäfer (2002) consists of clay and siltstone which are predominantly red in color. It can also contain sandstones and isolated calcoolites. This geological unit is divided into the Calvörde sequence and the Bernburg sequence.

The Calvörde succession (suC) is dominated by reddish claystone to siltstone with thin layers and banks of porous sandstone (oolithic calcareous sandstone). The Bernburg sequence includes oolitic calcareous sandstones of the main rogenstone zone with the 5 m - 6 m thick main rogenstone bank contained therein and an overlying alternating claystone-sandstone layer (formerly known as the Tonstein-Wechselfolge sequence) (BGE, 2018).

The Lower Buntsandstein only occurs on the northern flank of the Asse anticline (Szymaniak and Schäfer, 2002).

Middle Buntsandstein (sm)

BGE (2018) describes the Middle Buntsandstein as pale reddish to yellowish, poorly cemented sandstones with pelitic intermediate layers. This lithology results in a slight morphological accentuation in the terrain compared to both the Lower and the Upper Buntsandstein. The overall thickness of the Middle Buntsandstein is significantly reduced due to the absence of the upper Volpriehausen, Dethfurt and Hardegsen series in the area of study.

Upper Buntsandstein (so)

Szymaniak and Schäfer (2002) describes Upper Buntsandstein as predominantly colorful, partly marly shales, more rarely marlstone. The color of the mudstones alternates between red and green. The gypsum described in the boreholes, like the rock salt, were almost completely leached out on the surface. The weathering residues of the Upper Buntsandstein mainly consist of colorful, often green patches of clay.

This unit is confirmed by the Röt and Solling sequencies. In deep boreholes of the Lower Saxony Basin, the Röt can be divided into four sections (Röt 1 to Röt 4, so1 - so4). In Röt 1 and Röt 2, two horizons of sulphate rocks (anhydrite/ gypsum) appear, alternating with grey, greenish to violet-red clay/silt stones. The red rock salt is always subroded near the

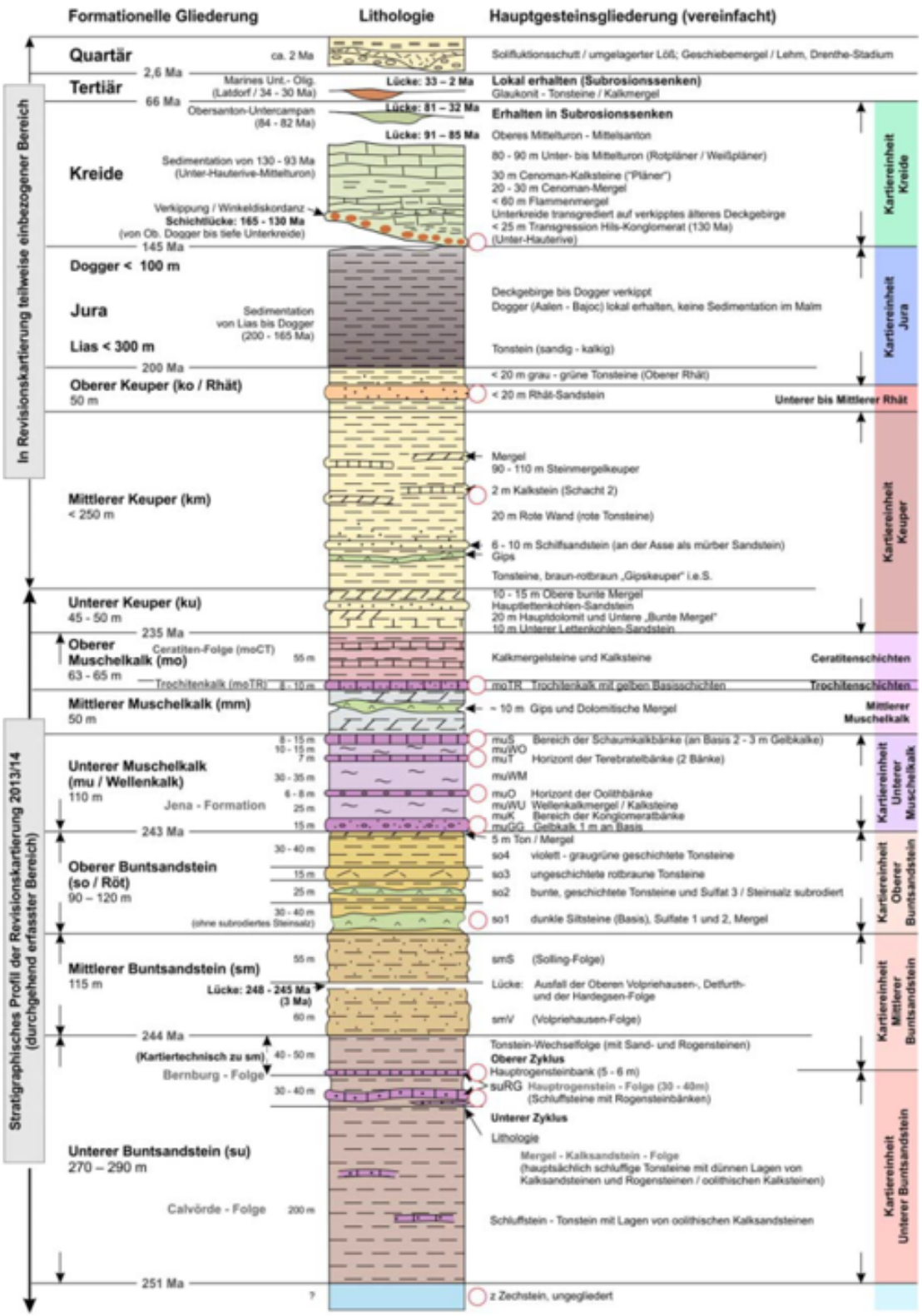

Figure 3.1: *Generalized stratigraphic column of the Mesozoic sequence (BGE, 2018).*

surface. The Röt 3 consists of massive, unstratified mudstones with discoloration haloes (reduction haloes). The Röt 4 consists of grey-green to violet mudstones, which are formed as yellow-grey to grey, marly mudstones on the last 5 m - 8 m before the shell limestone boundary. The Solling is a sequence of red sand and mudstones. The transition to the Lower Muschelkalk is indicated by the onset of limestone (BGE, 2018).

Lower Muschelkalk (mu)

The Lower Muschelkalk according to BGE (2018) consists of limestone formed in the shallow marine environment. The main rocks are thin-plate limestone with ripples ("wave limestone") and thin claystone layers, which are subdivided by banked conglomerate limestone (partly storm deposits, "tempestite"), which occur more frequently, especially in the lower area.

The up to 1 m - thick marly "Gelbkalk" (also "Gelbe Grenzbank", muGG) forms the base horizon. In addition to the "stone banks" (oolite, terebratula and foam limestone zones, immediately adjacent to the Middle Muschelkalk), there are other less thick limestone banks and numerous early diagenetically hardened layers (hard grounds). The oolite zone (muoo) is not represented in the area of the Asse-Heeseberg by the otherwise typical oolitic limestones, but by fine-grained gray limestone banks and yellow limestone embedded in this zone. The Terebratula Zone (muT) is approximately 7 m - thick. It includes two 3.2 m and 1.7 m - thick, diagonally stratified bank zones with clam shells and an approximately 2.5 m - thick wave limestone. After a further 10 m - 15 m of ripple limestone, the foam limestone zone (muS, 8 m - 15 m) begins with 2 m - 3 m - thick, fine-grained and layered yellow limestone (yellow limestone), followed by gray to yellowish and fine-grained limestone banks, the oolitic layers and shell-limestone. Due to the influence of meteoric waters (surface waters), further yellow limestones ("De-Dolomite") were formed by calcite incorporation from primary dolomites, which are concentrated in the oolite zone and at the base of the foamy limestone zone (BGE, 2018).

Middle Muschelkalk (mm)

The Middle shell limestone according to BGE (2018) consists mainly of yellow-greenish dolomitic marlstones. A sulphate horizon (approx. 10 m) occurs in the middle part of the Middle Muschelkalk. The Muschelkalk salt at the base of the horizon, which was also detected by deep drilling on the flanks of the Asse salt structure, has been deeply leached. Sinkholes in the outcrop area of the Middle Muschelkalk point by point mark the position of thicker sulphate/gypsum horizons lying close to the surface. Due to the ease with which it can be eroded, there are no natural outcrops in the Middle Muschelkalk. However, the dolomitic marlstones can be eroded at some steep trailheads.

Upper Muschelkalk (mo)

This unit is conformed by the Trochitenkalk and the Ceratiten successions. The Trochitenkalk succession according to BGE (2018) begins with 4 m - 5 m - thick, fine-grained yellow limestone, the "yellow base layers". These are followed by roughly stratified limestone banks containing trochites. In it are screes, oolite limestones and fine-grained hard grounds. In the course of the Asse-Heeseberg mountain range, a reduction in the overall thickness of the trochitebearing limestone beds from 8 m - 10 m in the NW to only 4 m - 5 m in the SE was determined (BGE, 2018).

The Ceratite succession according to BGE (2018) consists of thin, gray calcareous marlstones in alternating layers with dolomitic limestones and gray claystone layers. The boundary against the Keuper is formed by 10 m - 11 m - thick, calcareous mudstone ("clayey boundary

layers" of the Ceratite sequence). The 20 cm - 40 cm - thick cycloides bank typical of the Thuringian Basin, named after Coenothyris cycloides, is only vaguely developed. The eponymous Ceratites are rare in the Ceratite sequence of the Asse-Heeseberg ridge.

Keuper (ku, km, ko)

According to BGE (2018), the Keuper begins with the 10 m - thick "Unteren LettenKohlen-Sandstein", which consists of an alternating layer of gray to grey-green claystones with intercalated gray crumbly sandstone layers with partially strong mica layers. Above this are marlstone and sandy marlstone, as well as dolomite and sandstone in alternating layers. A further subdivision of the Keuper into Lower, Middle and Upper Keuper (ku, km, ko) and the identification of further lithostratigraphic horizons (e.g. main dolomite, main Lettenkohlensandstein etc.) is based on deep boreholes. Striking are light marl formations in the Middle Keuper and the approx. 20 m - 25 m - thick yellowish Rhät sandstones of the Rhät transgression of the Upper Keuper (Oberkeuper / Rhät, altogether approx. 50 m).

3.2.3 Jurassic (ju)

According to BGE (2018), the preserved Jura consists of gray mudstones with intermediate sandy layers and individual thin gray limestone layers. In it the Lias and Dogger groups can be distinguish. The Lias Formation consists of marine limestones, shales, marls, and clays. Dogger consists of mudstone, siltstone, sandstone. This unit preservation is reduced, also with gray mudstones, which occurs on both flanks of the Asse (BGE, 2018).

3.2.4 Cretaceous

Hils Conglomerate (kru), approximately 25 m - thick, represents the orange-colored calcareous-marly transgressive conglomerate of the Lower Cretaceous. It mainly consists of rounded edges of Muschelkalk (shell-bearing limestone) detritus, along with brown iron ore and Lias pebbles (BGE, 2018). It overlays the Jurassic sediments on the flanks of the Asse-Heeseberg with an unconformity of about 50 million years. This unit has an average thickness of 15 to 20 m but can locally reach up to approximately 25 m. Facies transitions to calcareous sandstones are observed.

Several occurrences of marine Upper Cretaceous deposits have been identified along the central main valley between the Asse I and Asse II shafts. These deposits consist of glauconitic claystones from the Upper Santonian and marly limestones from the Lower Campanian, both occurring in shallow beds (combined thickness up to 25 m). They overlay sulfates and carbonates of the Zechstein in subrosion depressions, as well as residual sediments of the Zechstein (BGE, 2018).

3.3 Description of the Röt Anhydrite B formation

The Röt-1 Anhydrite B (so1ANb) is a formation located on the southern flank of the Asse mine. It is the lowermost formation of the overburden on the southern flank. It belongs to the Upper Buntsandstein group, and it is followed by a sequence of clay and marlstone layers (Lower Muschelkalk). The Röt-1 Anhydrite B is approximately 14 to 16 m - thick and, in its normal conditions, a good aquiclude, meaning it has low hydraulic conductivity. This layer is not exposed at the surface of the study area due to the extreme tectonic stress in the near surface (GSF, 1996). According to Gärtner (2012), this unit forms the main pathway for the entry of fluids in the Asse II mine. The migration of the solution occurs through finely fragmented rock with a permeability of 10^{-14} to 10^{-16} m^2.

In general, anhydrite mineral occurs in evaporitic environments, in rocks of various ages, especially in limestone strata, and often the same that contain ordinary gypsum, and also very commonly in beds of rock-salt. Anhydrite mineral has the property that by absorption of moisture it changes to gypsum (Dana, 1922). In other words, when anhydrite and water interact, anhydrite recrystallizes as gypsum. This process involves swelling in the formation, with a volume increase of up to 60% (Chiesi et al. 2010; Steiner 1989, 1993, 2007 in Sass and Burbaum (2010))

In pure conditions, Anhydrite rock is characterized by its high density (approximately 2.8 to 3.0 g/cm^3) and non-porous nature. Anhydrite formations have higher P- and S-wave velocities that differ from other formations, such as rock salt (ranges from about 3 to 5 km/s for P-waves velocities) (Zong et al., 2023). Anhydrite is known to exhibit relatively low seismic attenuation, which means it can transmit seismic waves with minimal energy loss.

In Ludwig et al. (1998), ultrasonic measurements on minicore samples from boreholes were conducted to determine P- and S-wave velocities and their relationship to other physical properties, such as porosity and pore-shape distribution. The minicores samples were recovered at the Trans-Atlantic Geotraverse (TAG) hydrothermal mound. Some of their findings are:

- A general trend of increasing velocities with increasing densities can be observed for anhydrite samples.
- A trend is visible only for the anhydrite-rich rocks in general; seismic velocity decreases with increasing total porosity.
- Porosity effects on seismic velocities increase with higher anhydrite concentration of the rock.
- The ratio P-wave velocities to average S-wave velocities for the anhydrite-rich samples exhibits medium to high values ranging from 1.65 to 1.85.
- Increasing anhydrite concentration, v_p decreases linearly. Seismic velocities of the anhydrite-rich samples are substantially affected by the abundance of sulfate minerals. This is explained by an increase in anhydrite concentration, concentration of thin cracks, and vesicular pore spaces also increase. Both effects, the relatively low bulk moduli of anhydrite and the increase in small aspect ratio pore spaces, are the cause of this observed velocity/anhydrite concentration dependence.
- With increasing confining pressures applied to anhydrite samples, some cracks closed, and only partially reopened after pressures were reduced, resulting in velocity hysteresis between 5 and 20 MPa. This is also mentioned in Zivar et al. (2019). The hysteresis effect refers to the phenomenon where the behavior of a material depends on its loading and unloading history. In the case of anhydrite rock, the hysteresis effect can be observed in the porosity and permeability properties. During stress loading, the porosity of anhydrite core samples decreases, and during stress unloading, the porosity partially recovers but does not reach its initial value. This indicates that the closure of flow paths in the rock leads to a decrease in porosity, and the recovery is not complete during stress unloading. The hysteresis effect is more noticeable in anhydrite core samples compared to carbonate core samples.

Stress experiments conducted by De Paola et al. (2009) on borehole anhydrite samples showed that the permeability is initially very low, ranging from 10^{-21} to 10^{-19} m^2. However, during deformation, the permeability can increase significantly, reaching values ofup to 10^{-17} m^2. The increase in permeability is attributed to the development of a connected network of microcracks, both within and between grains. The permeability evolution differs between localized brittle failure and distributed ductile deformation, with higher

permeability increases observed during brittle failure at lower effective pressures. The establishment of a fully connected fracture network leads to a higher permeability rise during brittle failure compared to ductile failure. The permeability values attained at the end of the experiments are below 10^{-17} m^2 and are similar to previous results obtained from experiments on low-porosity rocks deformed in the brittle field (De Paola et al., 2009).

Furthermore, in other studies related with thin layers, Zong et al. (2023) highlight that the presence of a thin anhydrite caprock layer introduces a strong P-S-P event. This event comprises a P-wave within the overlying sedimentary formations, an S-wave within the anhydrite caprock, and another P-wave within the underlying salt body. This P-S-P event closely follows the primary P-wave transmission and exhibits a similar pattern to the primary P-wave reflection, particularly along the steep salt flank. This is remarkable since it generates artifacts in seismic data, which can lead to a misinterpretation of salt flanks.

Chapter 4

2D modeling of the Asse mine structure

The chapter presents the analysis of the 2D section of the study area. First, it stated the process of constructing the 2D model of the cross line 1545 (XL 1545), and further the analysis of exploding reflector test, which provide information in understanding the seismic signatures within the Asse mine structure.

4.1 Building the Model:

The base of the analysis lies in the data provided by BGE, particularly the interpreted horizons of the geological units along XL 1545 by seismic data interpretation. Utilizing this information, the geological model for the study section was created.

Additionally, data from borehole R5, located 55 m perpendicular from the study line, provided essential information. This borehole, drilled in 2022, is the deepest in the area, reaching a depth of 2300 m. With recorded P-wave velocity and density, and with the geological unit boundaries marks along this borehole, the P-wave velocity and density values were extracted for the geological units in study section (Fig. 4.1).

In XL 1545, geological units from the Paleozoic to the Cretaceous are identified. The geophysical parameters for the Jurassic, Cretaceous, and Rotliegend formations were derived from previous studies in the area (Sortan, 2022), as borehole R5 did not cross these units. Table 4.1 presents a list of all geological units in XL 1545 with their respective velocity and density values.

Considering the absence of further information on S-wave velocity (v_s) or its ratio with P-wave velocity (v_p), v_s was calculated following the rule of thumb $v_s = v_p/\sqrt{3}$. The S-wave velocity was derived empirically from the P-wave velocity, and the bulk density (Gardner et al., 1974).

With the geophysical parameters of P-wave velocity, S-wave velocity, and density in hand, the elastic wave equation for an isotropic medium was used for forward modeling. Unfortunately, the lack of extra information such as quality factor (Q_p) and anisotropic parameters (ε and δ) does not allow the use of a more realistic viscoelastic anisotropic wave equation in this study.

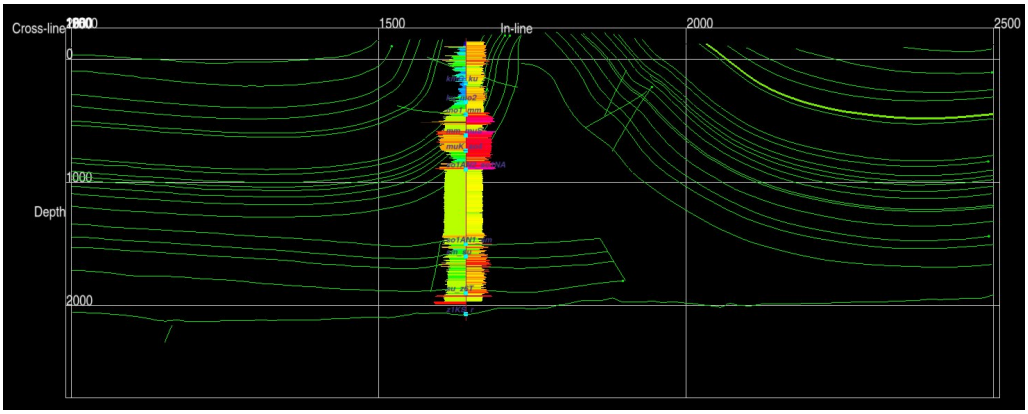

Figure 4.1: *Horizons XL 1545 (green) and data from borehole R5 (left velocity, right density).*

4.1.1 Parameters used for forward modeling using the software SOFI2D:

The dimensions of the model were set to 7200 m × 2600 m. An absorbing frame of 30 grid points was added to all sides of the model to prevent reflection from the model boundary. A grid size of 1 m were used resulting in a final model size of 7200 × 2600 grid points (Fig. 4.2).

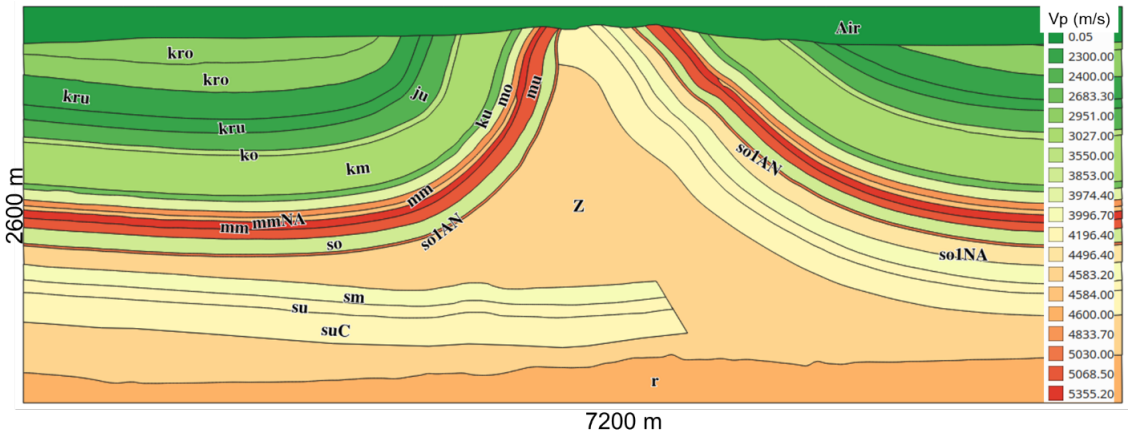

Figure 4.2: *Geological model for XL 1545.*

Receivers were placed following the model's topography, with a constant horizontal spacing of 10 m, totaling 697 receivers, with the first receiver at x = 50 m.

The simulation the minimum velocity corresponds to the velocity of the S wave of the unit Lower Cretaceous which is 1330 m/s, a maximum frequency of 100 Hz. For instance, in our simulation with a minimum wavelength of approximately 13.3 m, the recommended spatial grid spacing (Δh) was determined to be 1.663 m and we are using a grid size of 1 m.

Furthermore, in our simulation, we found that the Courant-Friedrichs-Lewy number was 0.5355, indicating stable conditions. With a maximum velocity 5355.20 m/s, we determined a stability limit for the time step to be 1.131781e-04 s and we are using a time step of 1 e-04 s.

Table 4.1: *Geophysical parameters of Asse mine structure.*

code	Formation	$v_p(m/s)$	$v_s(m/s)$	$\rho(kg/m^3)$
Air	Air	0.1	0.0	1.3
kro	Upper Cretaceous	2951.0	1735.9	2380.0
kru	Lower Cretaceous	2300.0	1330.0	2380.0
iu	Jura	2400.0	1385.0	2400.0
ko	Upper Keuper	3550.0	1547.5	2585.0
km	Middle Keuper	3027.0	1747.7	2200.4
ku	Lower Keuper	2683.3	1549.2	2183.2
ma	Upper Muschelkalk	3974.4	2294.6	2206.9
mm	Middle Muschelkalk	4833.7	2790.7	2724.7
manA	Muschelkalk -Steinsalz	4584.0	2646.6	2154.6
mm	Middle Muschelkalk	5355.2	3091.8	2773.8
mu	Lower Muschelkalk	5068.5	2926.3	2659.5
so	Röt	3853.0	2224.5	2584.8
so1ANb	Röt-1 Anhydrite B	5030.0	2904.1	2837.5
sm	Middle Buntsandstein	3996.7	2307.5	2164.4
su	Lower Buntsandstein	4196.4	2422.8	2295.4
suC	Calvörde-Formation	4196.4	2422.8	2295.4
z	Zechstein	4583.2	2646.1	2098.0
r	Rotliegend	4600.0	2706.0	2820.0

Exploding reflector test

In the exploration of the complex salt structure of the Asse, one of the critical questions that arose was the potential absence of rays reaching the surface from the Röt-1 Anhydrite B reflector in the dipping area of the south flank due to the high inclination of the layers. This raised the need to investigate whether seismic signals from the inclined part of the anhydrite interface could be detected on the surface. To address this question, the concept of the exploding reflector was employed, which offered a systematic approach to understand the behavior of seismic waves in such geological configurations.

The exploding reflector concept involves the placement of a dense array of seismic sources along the entire interface of interest, in this case the Röt-1 Anhydrite B reflector. These sources are simultaneously activated, generating seismic waves that propagate into the subsurface. The resulting seismic data provide insights into the behavior of waves as they interact with the geological structure, analogous to the behavior of a plane wave.

For this test, a total of 3532 seismic explosive sources were placed along the Röt-1 Anhydrite B interface on the south flank, covering its entire extent (Fig. 4.3). These sources were strategically positioned to ensure comprehensive coverage and maximize the information obtained from the seismic data. The sources were activated simultaneously, generating seismic waves that propagate into the subsurface.

The exploding reflector test allows to observe the zero-offset propagation of seismic waves, providing insights into how waves behave under this model. By analyzing the seismic data obtained from this configuration, it was able to determine the extent to which seismic signals from the inclined part of the Röt-1 Anhydrite B interface could be detected on the surface. The result of this simulation can be observed in Fig. 4.4.

Through forward modeling, we obtain snapshot sequences of seismic wave propagation and synthetic waveforms of the vertical and horizontal components along XL 1545.

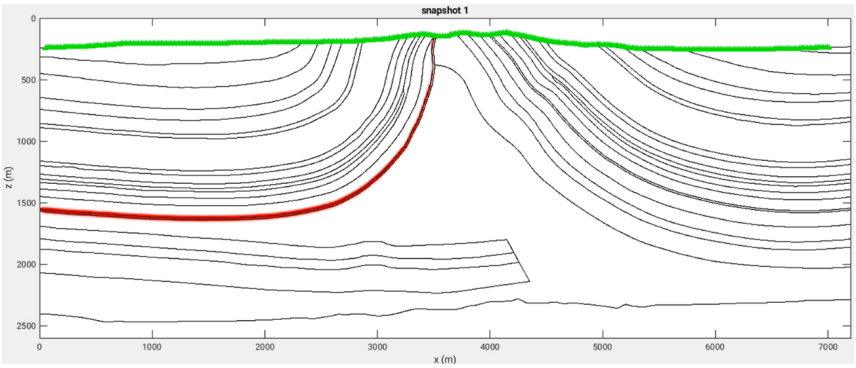

Figure 4.3: *Geological model, in red is marked the position of the sources.*

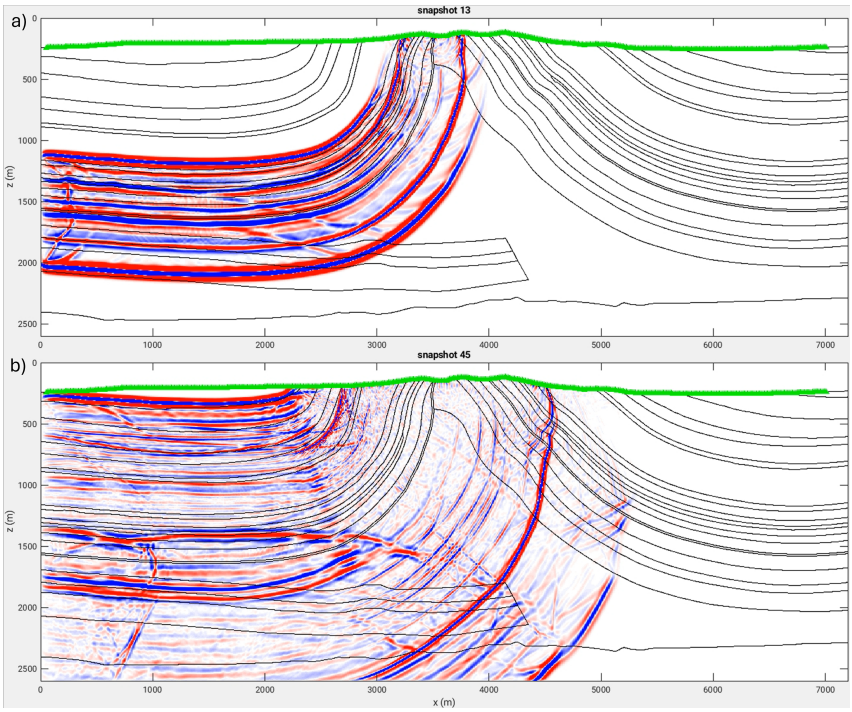

Figure 4.4: *Snapshot of the wavefield for the exploding reflector test for the vertical component. a) Snapshot 13 (t=0.13 s), b) Snapshot 45 (t=0.45 s).*

The vertical component snapshots are first analyzed. Figure 9 displays two snapshots: the first corresponding to the propagation of the P-wave occurring immediately after the sources were activated. Notably, receivers situated near the axis of the anticline towards the southern flank recorded the signal first. Subsequently, a secondary reflection occurred with the surface, leading to energy propagation downwards, causing multiples and a decrease in amplitude due to negative interference with subsequent wave reflections. In areas where the reflector is nearly vertical, the amplitudes recorded in the vertical component were low, as the energy predominantly propagated horizontally. Considering the polarization of the waves in this configuration, the vertical component record minimal energy in this area.

Snapshot 45 displays the arrival of almost all zero-offset reflections of P wave at the surface. With this test, it can be observed that zero-offset signals from any part of the dipping reflector could be anticipated for receivers placed approximately 1000 m horizontally from the anticlinal axis. Receivers positioned further from the axis would primarily record zero-offset reflections from portions of the Röt-1 Anhydrite B reflector located farther from the anticlinal structure, where the layer is nearly horizontal.

Fig. 4.5 presents snapshot 13 for the horizontal component, showing higher amplitudes of signals originating from the dipping reflector compared to the vertical component. This observation suggests that perturbations in the dipping area of the reflector may be more visible detected on the horizontal component. However, it is important to note that the seismic acquisition conducted in this area only recorded the vertical component, limiting the availability of horizontal component data in the field.

The exploding reflector test provided insights into the anticipated detection of zero-offset signals from the dipping Röt-1 Anhydrite B reflector in the Asse salt structure.

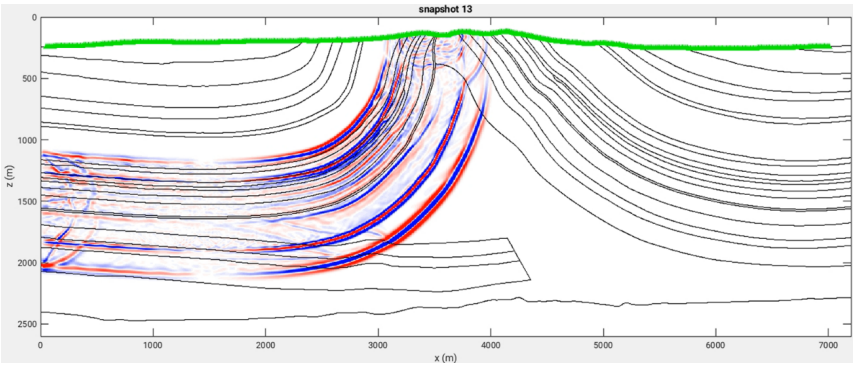

Figure 4.5: *Snapshot of the wavefield for the exploding reflector test (t=0.13 s), horizontal component.*

Chapter 5

Signatures of reflected elastic waves

Considering the hypothesis of this study, which suggests that fluids travel from the cap rock to the mine inflow point through the Röt 1 Anhydrite B Formation (So1ANb), this chapter aims to comprehend and analyze potential seismic signatures expressed by the upper and lower interfaces of this unit when the geophysical properties or geometry of the layer vary. The specific seismic response is investigated concerning reduced geophysical parameters (representing saturation of the layer), interference events due to layer thickness, and scattering effects, considering non-uniform fluid distribution within the layer.

To achieve this objective, a 2D model of three horizontal layers is constructed to analyze the upper and lower interfaces of the anhydrite layer (contact between Röt, Röt 1 Anhydrite B, and Zechstein) with a focus on the P - P wave reflection. This chapter presents the results of this analysis, utilizing data from borehole R5 located at 50 m from the study cross line with a depth of 2250 m, serving as the baseline model. The results are compared with other tests where various properties are varied.

5.1 Building the model

A three horizontal layers model is built with the dimensions of 7500 m horizontally and 2000 m vertically. The geophysical parameters (v_p, v_s, and ρ) assigned to this model were derived from borehole R5, where the properties of Zechstein geological unit correspond to the lower layer, the Röt 1 Anhydrite B layer corresponds to the middle layer, and the Röt unit corresponds to the upper layer (Fig. 5.1). This model is used and named the Base test.

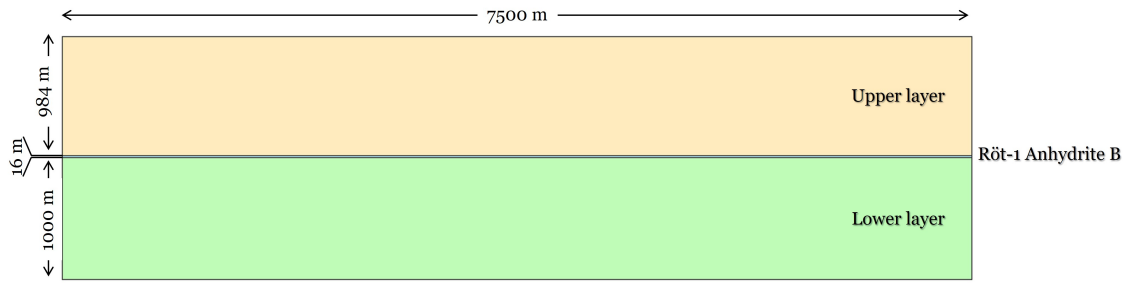

Figure 5.1: *Configuration of the three-layer model.*

Additionally, another test was created where the values of v_p, v_s, and ρ of the middle layer were reduced by 10%. This test aims to reflect the hypothesis that there are fluids in the Röt-1 Anhydrite B layer, therefore its geophysical parameters are reduced (Table 5.1).

Table 5.1: *Parameters for the rock units of the simplified model.*

Test name	Units	v_p (m/s)	v_s (m/s)	$\rho(kg/m^3)$
Base	so - Röt	3853.0	2224.5	2584.8
	so1ANb - Röt-1 Anhydrite B	5030.0	2904.1	2837.5
	Z - Zechstein	4583.2	2646.1	2098.0
Min10%	so - Röt	3853.0	2224.5	2584.8
	so1ANb - Röt-1 Anhydrite B	4527.0	2613.7	2553.8
	z - Zechstein	4583.2	2646.1	2098.0

With this configuration, the reflection coefficients and the tuning effect can be analyzed. Even though the reflection coefficients for each interface are independent of the thickness, when there are tuning effects, the superposition of the two interfaces causes the amplitude to change.

5.2 Reflection coefficients

The Zoeppritz equations provide reflection coefficients for both P-waves (compressional waves) and S-waves (shear waves) at the interface between the interest layer and the adjacent layers. These coefficients describe how much of the incident wave is reflected back into the upper layer and how much is transmitted into the lower layer. These coefficients can be used to understand the energy partitioning at the interface. The equations also describe the changes in amplitude and phase of the reflected and transmitted waves. Therefore, changes in the amplitude, phase, and critical angle of the seismic waves could be indicator of fluids in the layer.

The Zoeppritz equations were calculated for the upper and lower interface for the Base and the Min10% test (Fig. 5.2).

As a result, for the top interface, in both the Base and the Min10% test, the velocity below this interface is higher, therefore refracted waves are generated at a critical angle of 50° and 58° respectively. It is evident that when the parameter values of the second layer increases, the critical angle decreases, and the amplitude of the reflection coefficient increases before the critical angle.

For the lower interface in the Base test there is a higher velocity layer above a layer with lower velocity, therefore refracted waves are not developed. Nevertheless, for the Min10% test there is a critical angle at approximately 80° due to the velocity slightly increases in the lower layer.

The amplitude of the coefficients increases when the contrast of the parameters in the interfaces increase.

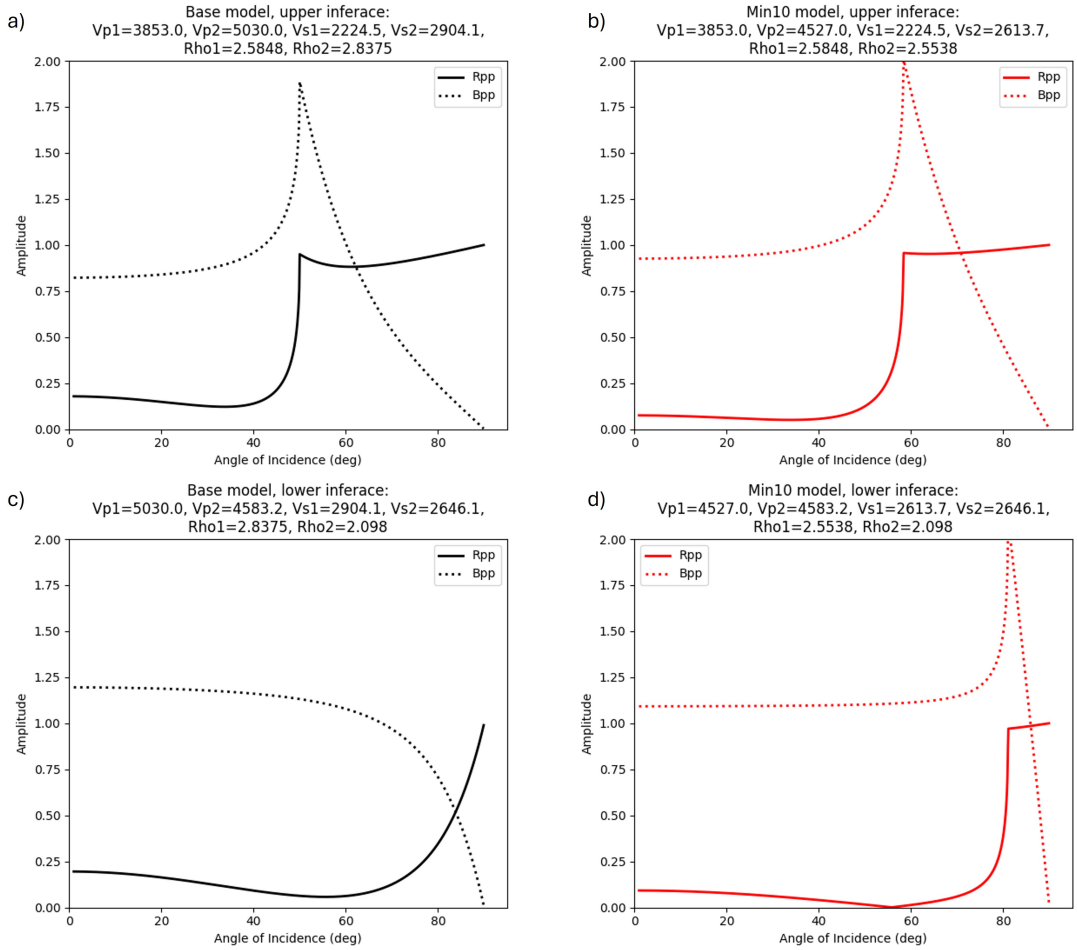

Figure 5.2: *Absolute reflection and refraction P-P coefficients of the upper and lower interfaces of the Röt-1 Anhydrite B layer (R=reflection coefficient, B= refraction coefficient). a, c) for the Base test, and b, d) for the Min10% test.*

5.3 Tuning effect

The main effect of tuning is that the top and base events of a thin layer overlap each other and cannot be separated due to low seismic resolution. Therefore, a single event of high amplitude can be observed on seismic data.

A wedge-shaped geological model is created with three layers, taking into consideration a range of thickness of the Röt-1 Anhydrite B layer. This is modelled for both the Base and Min10% test. The synthetic gathers are analyzed at zero offset for different thickness.

Fig. 5.3 indicates that in general for both tests, the amplitude increases with an increase in thickness up to a maximum, where the tuning thickness is reached and then it decreases in amplitude up to approximately 40 m thickness. However, when the thickness increases from 40 m, amplitude response becomes flat, which indicates that seismic reflections from the top and base of the wedge are not interfering.

For the tests where the parameters of the middle layer were reduced with respect to the Base test the tuning thickness is smaller, and its amplitude is reduced as well. It could tell us that if the geophysical parameters of the thin Röt-1 Anhydrite B layer are reduced it would be harder to see the separation of the top and base interface at smaller thickness.

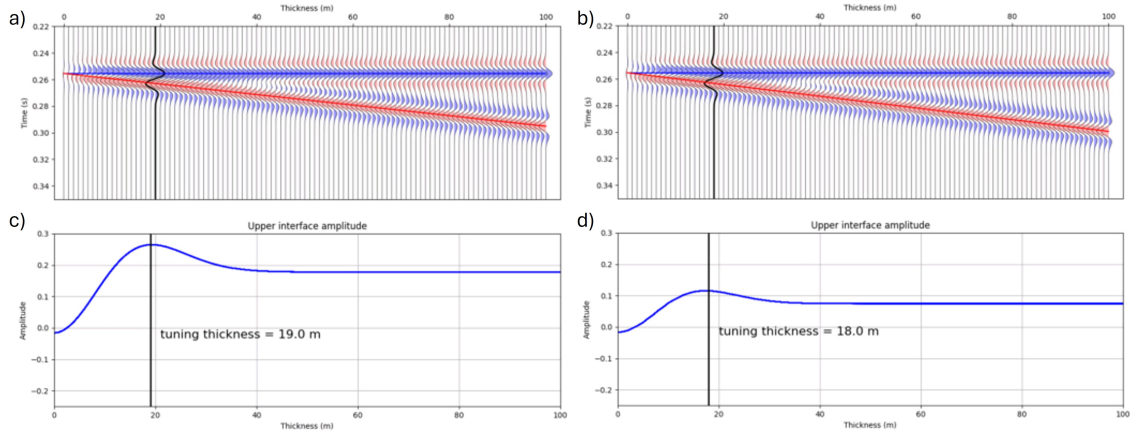

Figure 5.3: *Three-layer model with the parameter values for the base test (a, c) and Min10% (b, d) tests and frequency of 50 Hz. a, b) Synthetic seismogram by using zero offset Ricker wavelet of 50 Hz frequency. c, d) Amplitude of synthetic seismogram showing maximum response thickness.*

5.4 Forward modeling

To understand the specific response to various effects that may occur in seismic data, different tests were designed. Starting from the most basic premise, the problem was framed around the hypothesis that fluids could be traveling through the 16 m thick anhydrite layer. This raised questions about the seismic signature of the event as the wave passes through the upper and lower interfaces of the thin anhydrite layer and how the response changes when parameters are reduced to simulate fluid presence. Additionally, there was a query regarding the seismic response if fluids in this layer were not uniformly distributed but localized in a single zone.

To address these questions, forward modeling using the finite difference method was employed. This method approximates solutions to differential equations, such as the wave equation, which governs the propagation of seismic waves in the Earth.

Different tests were formulated to analyze the seismic response of each of the aforementioned questions. For example, one test modeled the three layers with baseline parameters and a middle layer thickness of 16 meters (Base_16m). This was compared with another test with the same parameters but a middle layer thickness of 80 meters (Base_80m), where tuning effect is absent. This comparison allows observing the seismic signal when tuning effect is present and when it is not.

Additionally, to observe the specific seismic signatures resulting from the reduction in the geophysical parameters of the anhydrite layer, two other tests (Min10%_16m and Min10%_80m) were designed with parameters reduced by 10% compared to the baseline.

To analyze the seismic response considering non-uniform fluid distribution, a test was created based on the Base_16m test, introducing an ellipse-shaped perturbation in the center of the anhydrite layer with parameters from the Min10% test.

Fig. 5.4 shows a sketch of the different tests geometry model, and the Table 4 shows the parameters used for each test.

As mentioned above, the model rock-parameter relations were created based on the borehole data provided by BGE. Below are the configuration parameters used for the forward modeling using the program SOFI2D.

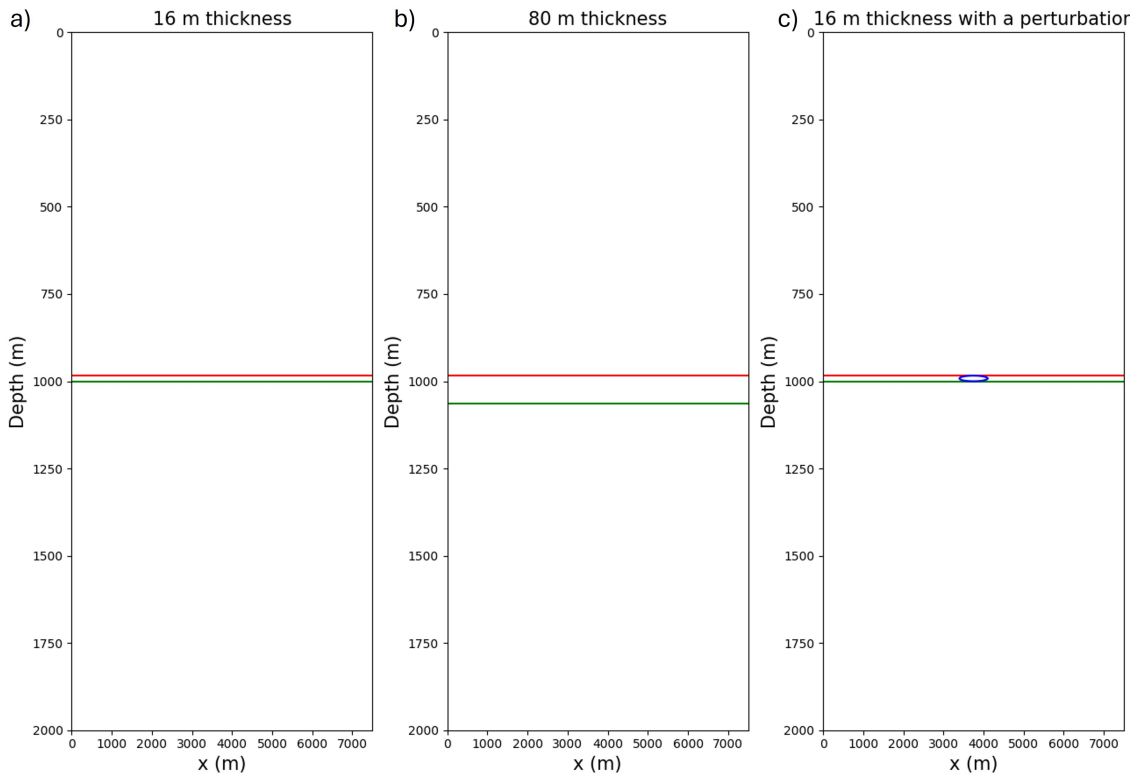

Figure 5.4: *Configuration of the models. a) middle layer with thickness of 16 m. b) middle layer with thickness of 80 m. c) model with the ellipse perturbation, for this model the source were places at X=3750 m.*

- Grid spacing: 1 m.
- Time of wave propagation: 5 s.
- Sampling interval of output data: 0.000500 s.
- Wave equation: elastic isotropic.
- Time step interval (DT): 1.0e-04 s.
- Central frequency: 50 Hz.
- Source:
  - Shape: Ricker
  - Type: force in y
  - Location x: 55 m
- Receiver: in total 741 separated each 10 m. Position of the first receiver is 50 m.
- Absorbing frame:
  - Width of absorbing frame (FW): 30 grid points
  - Type of frame (ABS_TYPE): CPML

In the next sections, it is explained how the obtained tests were processed, followed by their analysis.

5.4.1 Processing the data

Keeping in mind that the focus of this study is the P-P reflection wave, it is necessary to eliminate direct and superficial waves since they create noise in the seismic data for this analysis, making it more difficult to identify the relevant waves.

In order to extract the unique signal of both the direct and superficial waves, a version of only the first layer was modeled (Fig. 5.5).

Table 5.2: *Parameters for each test.*

Test name	Units	v_p (m/s)	v_s (m/s)	ρ (kg/m^3)	t	Source position
Base_16m	so - Röt	3853	2225	2585	984	
	so1ANb - Röt-1 Anhydrite B	5030	2904	2838	16	x = 55 m
	z - Zechstein	4583	2646	2098	1000	
Min10%_16m	so - Röt	3853	2225	2585	984	
	so1ANb - Röt-1 Anhydrite B	4527	2614	2554	16	x = 55 m
	z - Zechstein	4583	2646	2098	1000	
Base_80m	so - Röt	3853	2225	2585	984	
	so1ANb - Röt-1 Anhydrite B	5030	2904	2838	80	x = 55 m
	z - Zechstein	4583	2646	2098	1000	
Min10%_80m	so - Röt	3853	2225	2585	984	
	so1ANb - Röt-1 Anhydrite B	4527	2614	2554	80	x = 55 m
	z - Zechstein	4583	2646	2098	1000	
Base_16m	so - Röt	3853	2225	2585	984	
	so1ANb - Röt-1 Anhydrite B	5030	2904	2838	16	x = 3750 m
	z - Zechstein	4583	2646	2098	1000	

Subsequently, this version was subtracted from all tests to denoise them (Fig. 5.6). This methodology was employed to prevent alterations in the amplitudes or waveform that might be introduced by other methods.

Reflected seismic waves on a common midpoint (CMP) gather when plotted in the time-offset domain present a pattern of a hyperbolic curve. This is a characteristic pattern observed in seismic data, especially for reflections from point diffractors or interfaces with simple geometries as is the case in our three horizontal layers model.

Moveout refers to the change in arrival time of seismic reflections as a function of offset. To create a clearer and more interpretable seismic image, the data needs to undergo moveout (MO) correction. In this study hyperbolic moveout pattern is corrected to obtain a flat or nearly flat response in the time-offset domain, making it easier to interpret and analyze the seismic data through different angles or offsets.

The time it takes for a seismic wave to travel from the source to the subsurface interface and back to the receiver depends on the depth of the interface and the offset from the source-receiver midpoint. Thus, the hyperbolic moveout equation is often expressed as:

$$t^2 = t_0^2 + \frac{4h^2}{v_{\mathrm{NMO}}^2} \tag{5.1}$$

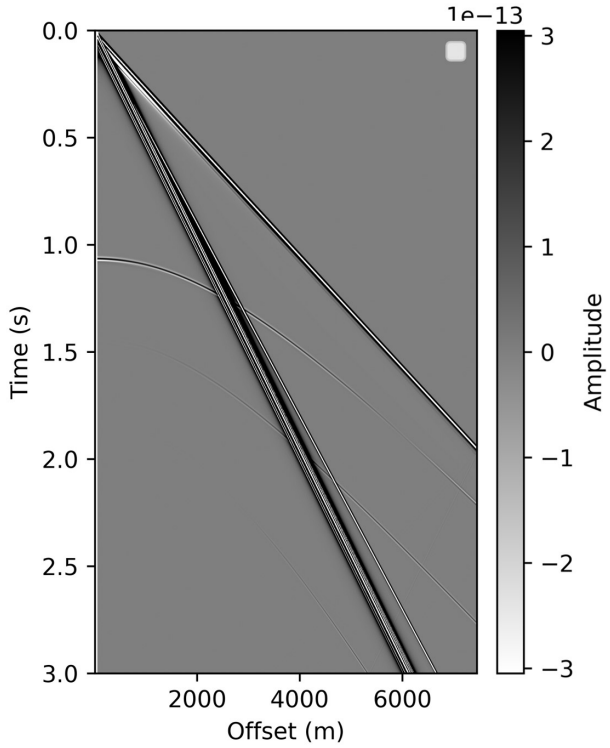

Figure 5.5: *Shot gather of the synthetic seismic data modeling the ground roll and direct wave. Source located at x = 55 m (receiver spacing 10 m).*

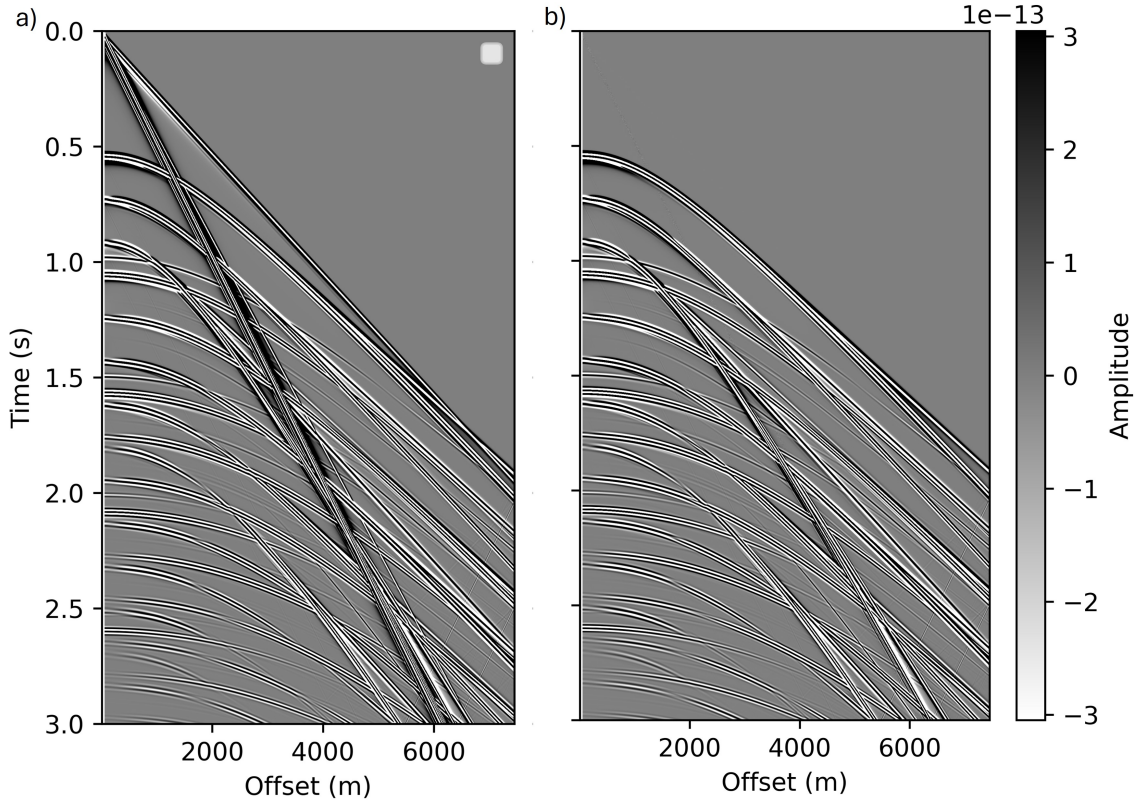

Figure 5.6: *Shot gather of the synthetic seismic data noise removal. Source located at x=55 m (receiver spacing 10 m). a) full shot gather, b) shot gather without noise.*

where t is the two-way travel time, t_0 is the zero-offset time (travel time at zero offset), h is the offset distance, v_{NMO} is the normal moveout velocity.

This equation allows one to calculate the time shift for each offset over the initial time. Once it is calculated, this time shift is subtracted from the initial time for each offset (Fig. 5.7). This can be applied since the velocity in the layers is constant and the interfaces are horizontal.

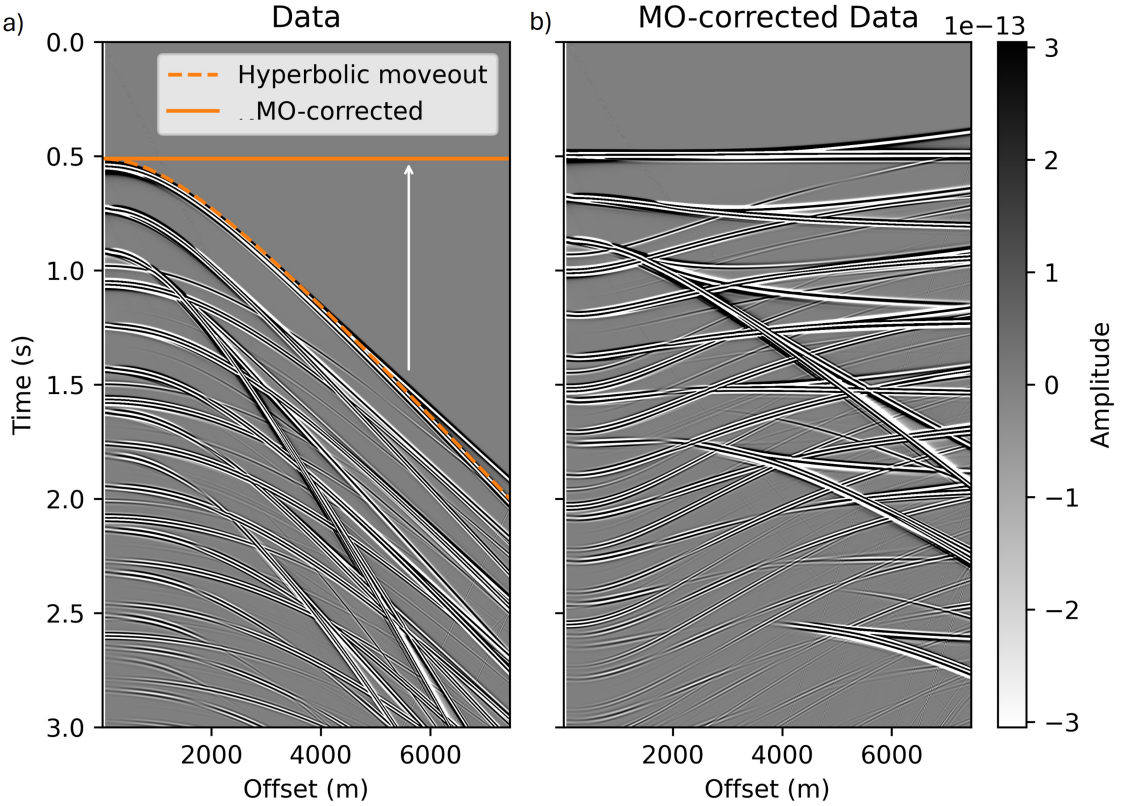

Figure 5.7: *Hyperbolic moveout correction.*

Fig. 5.7 shows an example of the MO correction of the synthetic data. As is observed in the figure, this correction was performed for the P-P reflection, therefore, the other events are not corrected and present curved shapes.

5.4.2 Synthetic test results

As previously stated, several tests were conducted. We analyze the differences between them when specific attributes change in this section. The focus of this examination is P-P reflection.

The finite difference modeling results for the test are presented in the following figures (Fig. 5.8 to Fig. 5.10). In the upper part of each figure, a plot showing variations in the maximum amplitude of the event across different angles of incidence is presented. Additionally, the lower part of the figures displays the angle gather for the specified test.

Tuning Effect Analysis: Fig. 5.8 present comparisons between angle gathers obtained from the three-layer model with variations in the thickness of the middle layer. Specifically, Fig. 5.8a illustrates the “Base_16m” test, where the middle layer has a thickness of 16 m, while Fig. 5.8b showcases the “Base_80m” test, featuring a thicker middle layer of 80 m.

Notably, a distinct contrast emerges between the two tests, particularly noticeable for near offsets, before the critical angle.

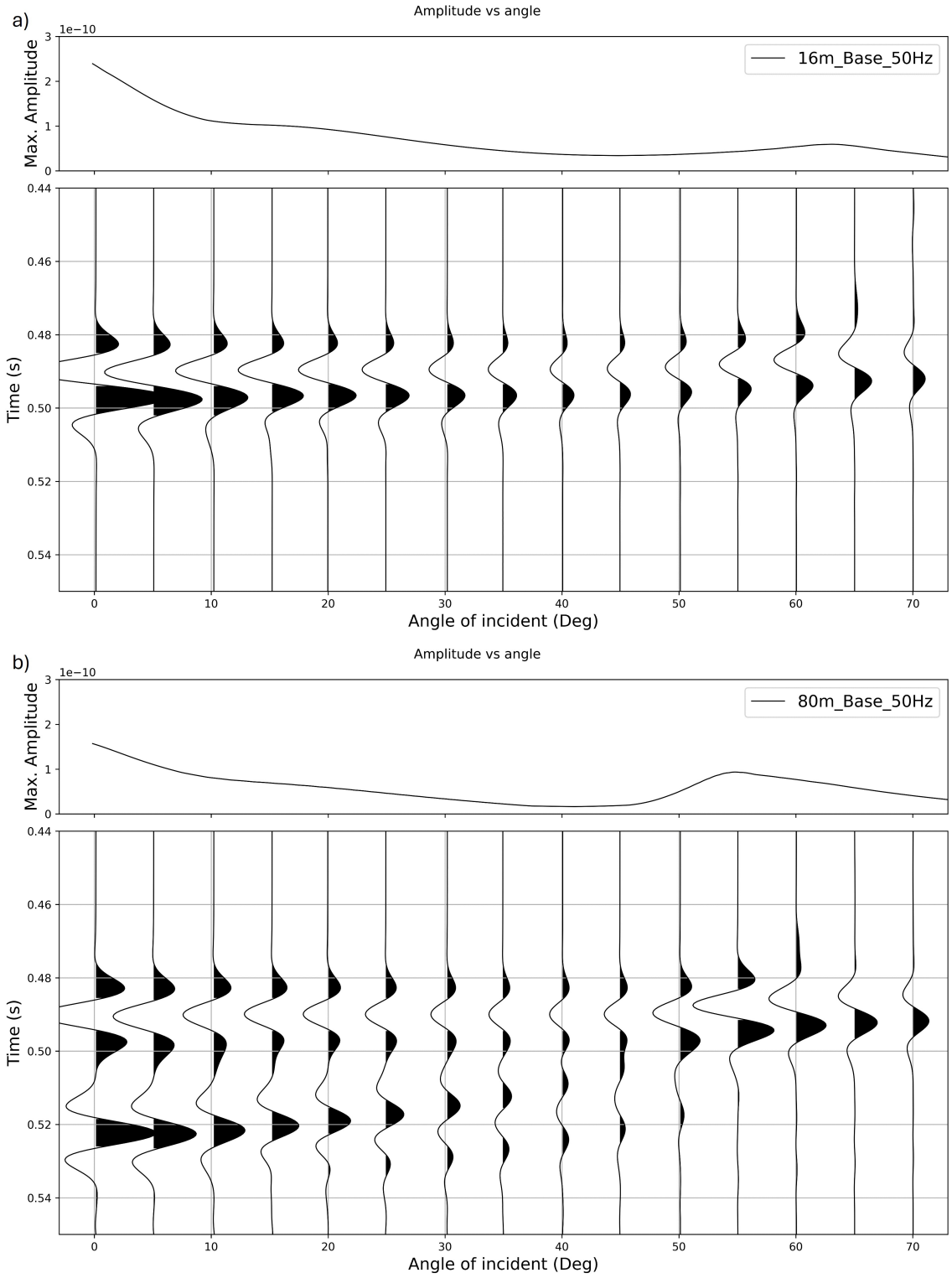

Figure 5.8: *a) Synthetic angle gathers for the test where the middle layer is 16 m thick. b) Synthetic angle gathers for the test where the middle layer is 80 m thick.*

In the "Base_16m" test, the tuning effect becomes evident due to interference between seismic responses of the upper and lower interfaces of the middle layer. This interference

results in an increase in the absolute amplitude of the seismic signal for low incident angles, accompanied by waveform changes. Conversely, in the “Base_80m” test, where the layer's thickness is sufficient to avoid the tuning effect, the seismic responses of the upper and lower interfaces can be distinctly observed and separated. Despite substantial similarity in seismic responses for far offsets between the two tests, there is a notable decrease in amplitude when the tuning effect is present.

The critical angle, approximately 50^{o} for both thickness tests, remains unaffected by the tuning effect, indicating that while the tuning effect may alter seismic signals, it does not directly impact the critical angle of seismic waves.

Parameter Reduction Analysis: Fig. 5.9 extend the comparison to include tests where parameters are reduced by 10% (shown in red). Here we can observe, when parameters are reduced, changes occur mainly in the amplitude of seismic signals, with minimal differences in arrival time and no waveform alteration observed.

For angles below the critical angle, the reduction in density and velocity of the middle layer leads to a decrease in amplitude compared to the Base test, along with a time shift. Conversely, for angles near and above the critical angle, the amplitude slightly increases in the model with reduced parameters compared to the Base tests.

These differences are more pronounced in tests with an 80 m thickness of the middle layer, primarily because the upper and lower interface signals do not interfere, and the wave travel time through the middle layer is longer.

Scattering Effect Analysis: Further analysis considers the scenario where fluids are not uniformly distributed throughout the layer but concentrated in a specific area. A test with a perturbation in the middle of the anhydrite layer resembling an ellipse with a maximum radius of 350 m and a minimum radius of 16 m is conducted. The geophysical parameters of this perturbation correspond to those in the Min10% test, with the source placed directly above the perturbation. This perturbation introduces additional complexities in the seismic response due to the scattering effect (Fig. 5.10).

Fig. 5.10 compares the Base_16m test (black) with the test incorporating the perturbation (red). Areas with the perturbation exhibit reduced amplitude and minor time shifts. Additionally, reflections from the perturbation boundaries result in additional wiggles in the seismic signal due to the scattering effect. When the wave encounters the perturbation, the wavefront becomes distorted, and energy deflects in various directions, as a result we obtain a more complex signal. However, the amplitude of signals generated by the scattering effect is low, even in synthetic data without the presence of noise. Making it difficult to track this effect in the field data.

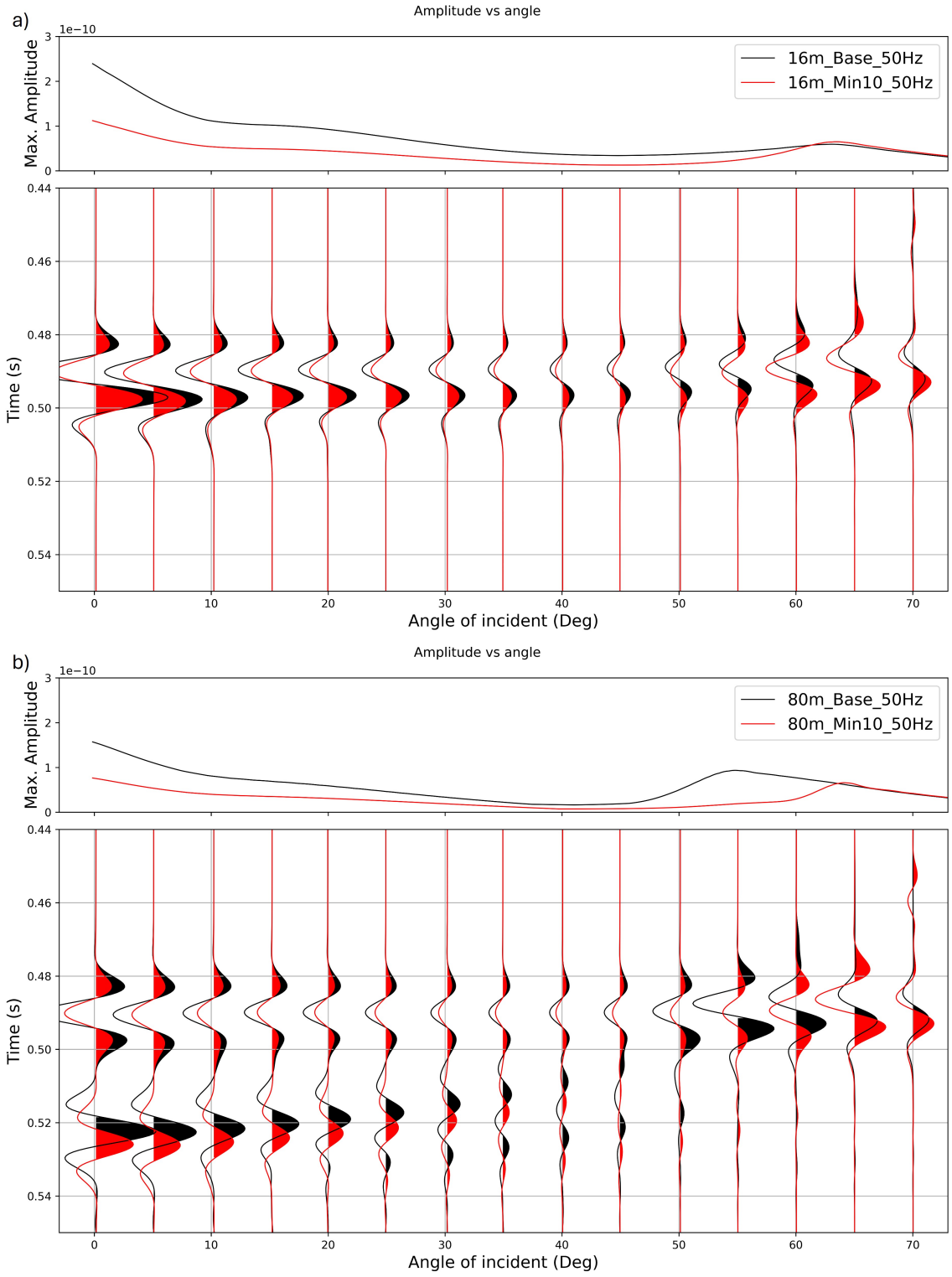

Figure 5.9: *a)Synthetic angle gathers for the 16 m middle layer thickness. In black Base_16m test and in red the Min10%_16m test. b) synthetic angle gathers for the 80 m middle layer thickness. In black Base_80m test and in red the Min10%_80m test.*

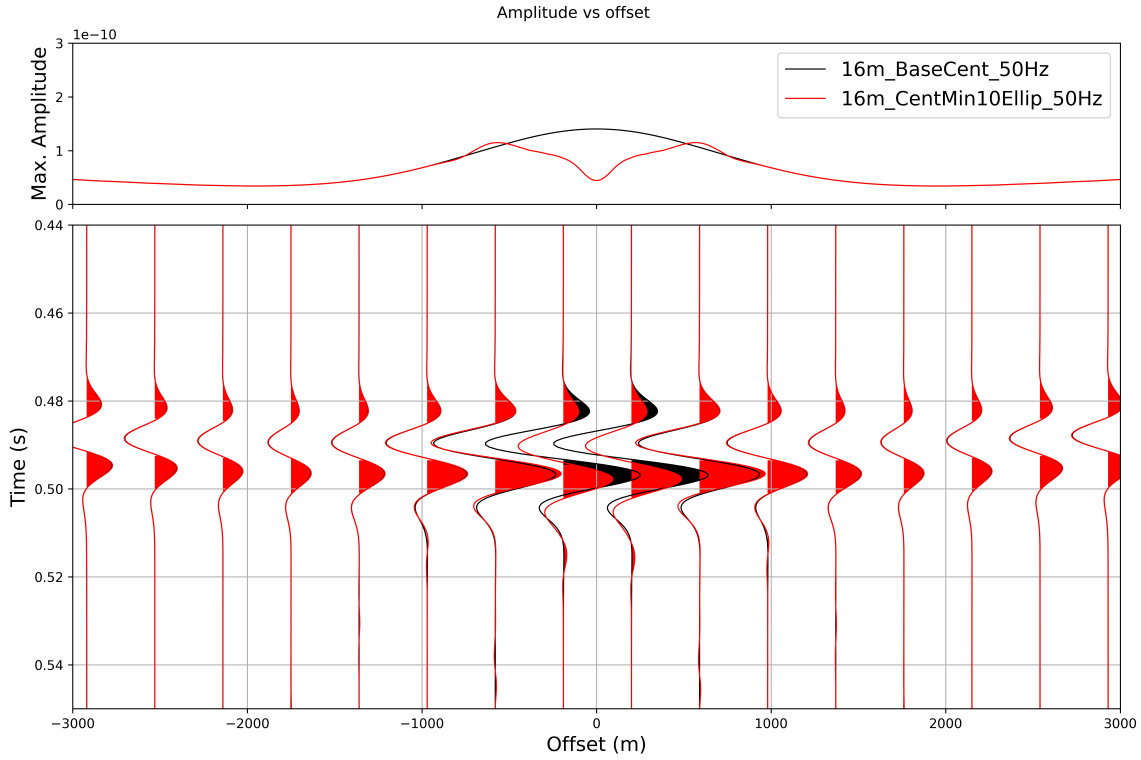

Figure 5.10: *Synthetic angle gathers for the 16 m. In black Base_16m test and in red with a perturbation in the middle of the model.*

Chapter 6

Field data observations

In this chapter, we examine the field data supplied by BGE. We aim to investigate seismic responses in the field data and analyze if any observed patterns or characteristics correlate with the observations in synthetic data. By doing so, we aim to enhance our understanding of the geological and geophysical complexities in the study area. For this we analyzed post migrated gathers and stacks at various dip angles and frequencies.

6.1 Description of the migrated field data

The post-stack depth migrated angle gathers and stack used for this analysis are an extraction of the Asse field data provided by BGE. The Earth Study 360 migration tool was used for the imaging. The polarity convention of the data aligns with the Society of Exploration Geophysicists (SEG) European Standard, where an increase in impedance corresponds to a minimum in amplitude. The data are zero-phase and azimuth is defined against North.

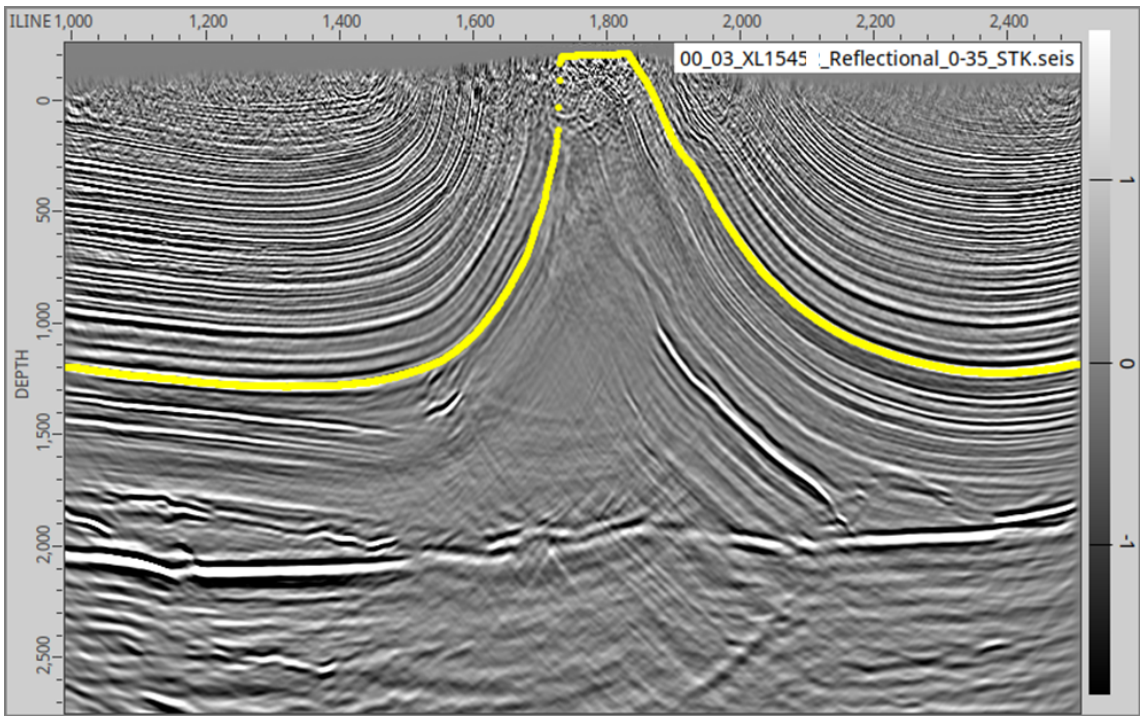

Figure 6.1: *Migrated field data, stack 0° -35°, highlighted the Röt-1 Anhydrite B event.*

Fig. 6.1 displays the migrated stack covering a dip angle range from 0° to 35° for XL 1545. The orientation of the image is such that the left side points towards the southwest, while the right side points towards the NE. Here all depths referenced are below sea level . In the central region of the image, the salt dome structure is visible, spanning from approximately 0 m depth to 2100 m. The chambers at the mine are situated at depths ranging from approximately 300 m to 600 m, next to the south flank. The first inflow point registered in the mine was located at a depth of about 300 m, and currently the fluids are collected at a depth of about 400 m.

As previously noted, the anhydrite interface is characterized by a minimum in amplitude, indicating an increase in impedance (depicted as a black event). Along inline 1000, this interface is located at a depth of 1195 m. (Fig. 6.1 and Fig. 6.2).

It is important to highlight that towards the upper part of the dome, the image experiences a loss of resolution, posing challenges in tracking the Röt-1 Anhydrite B interface towards the dome's upper section. The following analysis will focus mainly on the steeply part of the anhydrite reflector at the south flank (Fig. 6.2).

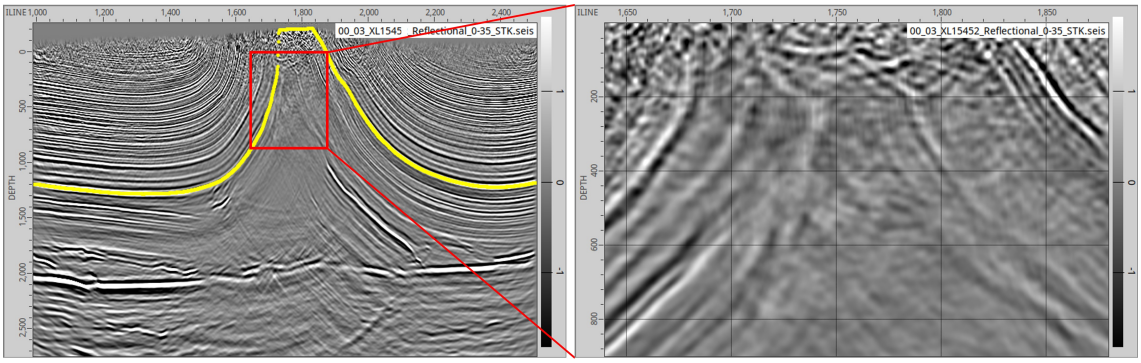

Figure 6.2: *Zoom of the area of focus. Migrated field data, stack 0° -35°.*

6.1.1 Dip angle stack

Angle stacks serve as useful tools for assessing reflectivity at specific incidence angles, providing insights into the behavior of seismic waves as they interact with subsurface structures.

Dip-angle gathers are subsets of seismic data organized based on the angle of incidence, or dip angle, at which seismic waves hit reflectors. By categorizing data according to dip angle, analysts can investigate how seismic reflections vary across different angles of incidence, offering information for the interpretation at subsurface geological features and to determine a rock's fluid content, porosity, density or seismic velocity.

In this analysis dip angles ranges (stack) were used because the the signal to noise ratio was to poor to analyse the gather. This in order to look at the behavior of the data at different incidence angles and observe how the Röt-1 Anhydrite B event is enhanced within these ranges.

We stacked the data into the following dip angle intervals: 0° to 5°, 5° to 10°, 10° to 20°, 20° to 40°, and 40° to 80° (Fig. 6.3).

Upon initial observation, it is evident that the resolution within the focal zone is generally low, particularly towards the top of the southern flank of the salt dome (approximately at a depth of 0 meters), making it challenging to track the Röt-1 Anhydrite B reflector.

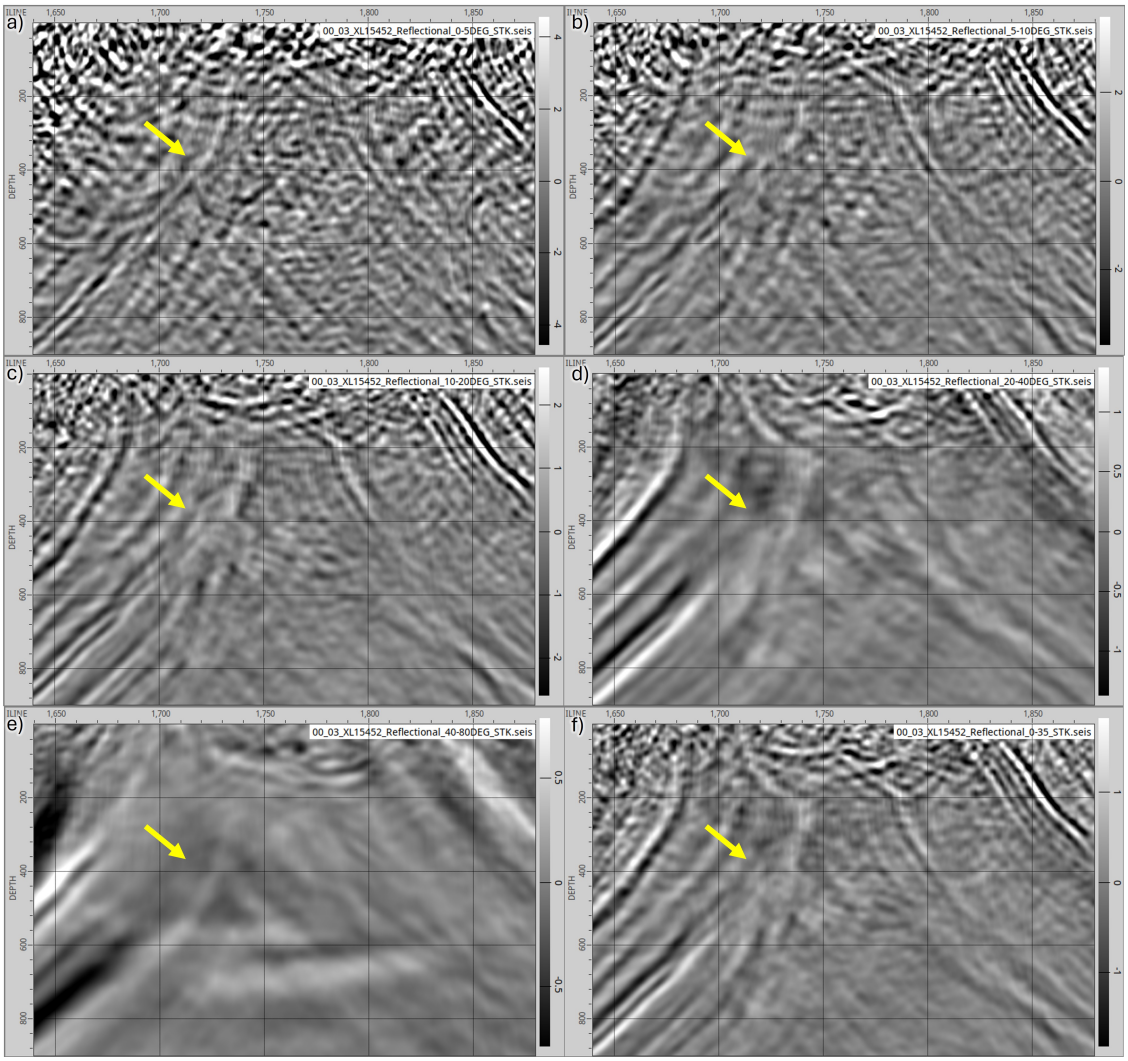

Figure 6.3: *Dip angle stack data. a) 0° to 5°, b) 5° to 10°, c) 10° to 20°, d) 20° to 40°, e) 40° to 80° and f) 0°- 35°.*

When examining the stacked data for dip angles between 0° to 5°, we observe significant noise in the image, but the anhydrite event can be traced to a depth of approximately 100 m.

For to dip angle ranges of 5° to 10° and 10° to 20°, the amplitude of the anhydrite event decreases considerably, making it difficult to track this event. For higher dip angles (20° to 40° and 40° to 80°), the anhydrite event becomes increasingly blurry and indistinguishable.

Focusing specifically on the anhydrite event, we note that it becomes more prominent at lower dip angles, particularly in the range between 0° to 5° (Fig. 6.4). However, the decrease in Signal-to-Noise Ratio (SNR) at low dip angles impacts the clarity of surrounding events.

6.1.2 Frequency stack

In seismic data analysis, band-pass filtering plays an important role in selectively preserving frequencies within a specified range while minimizing distortions to the original signal. The bandwidth of the filter, defined by the gap between its higher and lower cutoff frequencies, determines which frequencies are retained. Examining various band-pass filters within the

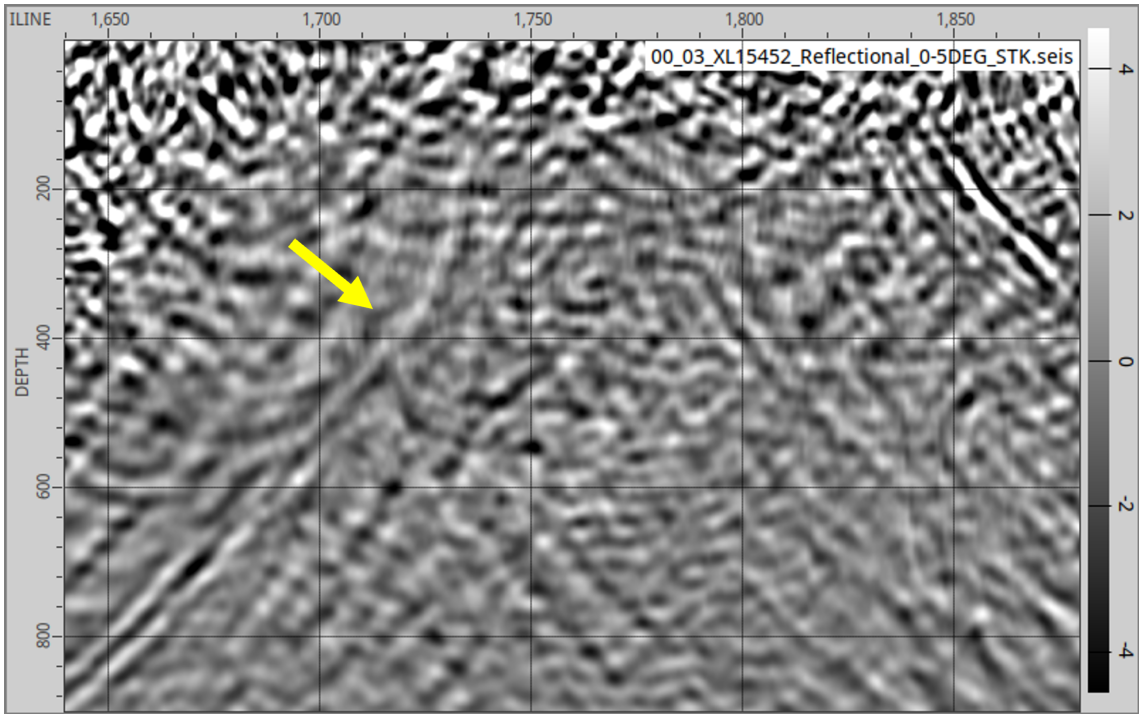

Figure 6.4: *Angle stack from 0° to 5°.*

context of reflection seismic data helps to the quality and interpretability of seismic images.

Similarly to the approach taken for different dip angles, we applied multiple consecutive band-pass filters to the field data to investigate the frequency range in which the enhancement of the anhydrite interface is most prominent (Fig. 6.5). From our observations from the dip angle analysis, we based our analysis on the dip angle range of 0° to 5°, where the anhydrite event was most prominent.

The selected frequency ranges for band-pass filtering were 0 Hz to 10 Hz, 10 Hz to 20 Hz, 20 Hz to 40 Hz, 40 Hz to 80 Hz, and 80 Hz to 120 Hz. This selection aimed at identifying the frequency band where the anhydrite event exhibits optimal enhancement.

Upon close examination of the anhydrite interface, we observed the following:

- In the low-frequency range of 0 Hz to 10 Hz, the resolution is notably low, and the data is noisy, making it challenging to identify the anhydrite event (Fig. 6.5a).
- In the frequency ranges of 10 Hz to 20 Hz and 20 Hz to 40 Hz, the anhydrite event becomes more visible, with the interface traceable up to depths of approximately 200 meters.
- However, as the frequency increases to 40 Hz to 80 Hz and 80 Hz to 120 Hz, the amplitudes of the anhydrite event decrease, leading to difficulties in identification.

Based on our observations, the frequency range between 10 Hz to 50 Hz with dip angle between 0° to 5° appears to offer the most favorable conditions for enhancing the visibility of the anhydrite layer (Fig. 6.6). This frequency band provides better resolution and amplitude for identifying and tracking the anhydrite event within the field seismic data.

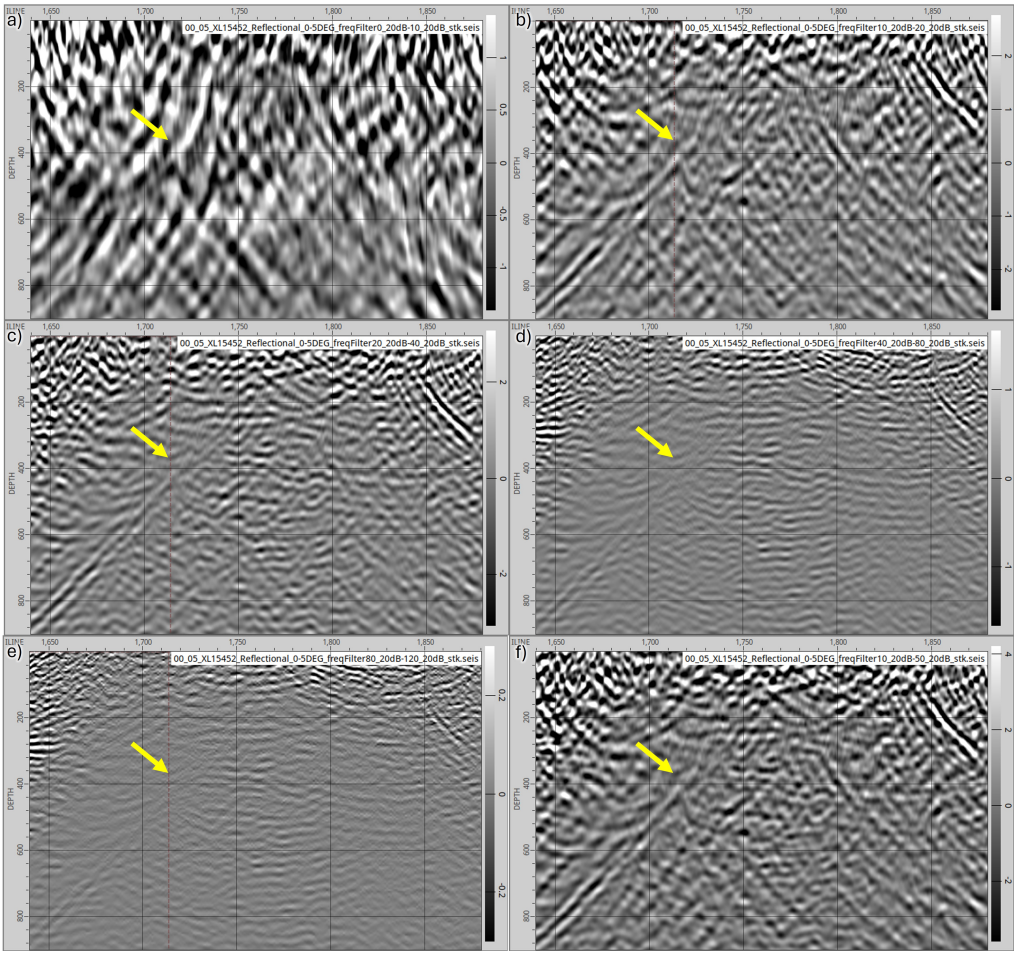

Figure 6.5: *Stacked data utilizing band-pass filters across different frequency ranges are displayed for angle stack from 0° to 5°. a) 0 Hz to 10 Hz, b) 10 Hz to 20 Hz, c) 20 Hz to 40 Hz, d) 40 Hz to 80 Hz, e) 80 Hz to 120 Hz, and f) 10 Hz to 50 Hz*

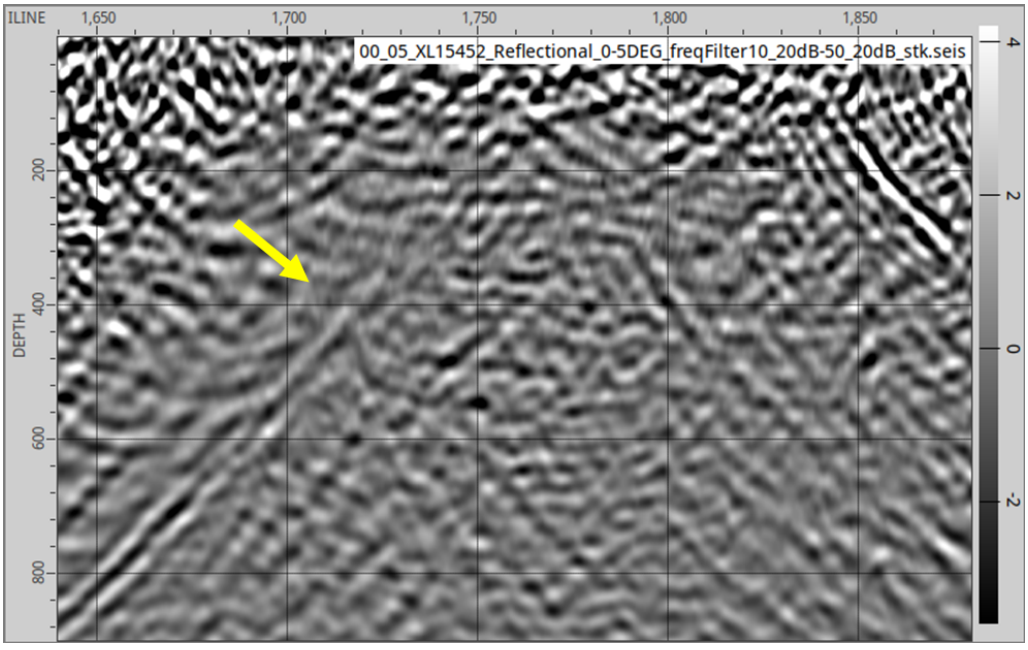

Figure 6.6: *Bandpass filter of 10 to 50 Hz and 0°-5° dip angle stack.*

6.2 Discussion

Seismic imaging of vertical or near-vertical reflectors in our study area presents considerable challenges due to a multitude of factors contributing to the complex wave propagation patterns and seismic responses observed. The intricate nature of these reflectors can lead to wave energy being refracted, reflected, or diffracted in unpredictable ways, resulting in smeared and blurred seismic events during data stacking. These challenges are further compounded by geological features, such as high-velocity-contrast units where the velocity inversion from the Muschelkalk to the Röt complicates the wave field due to the generation of guided waves, and fractured rock formations, which introduce additional complexities to the seismic response. Moreover, the focus area is situated in close proximity to the cap rock, adding more complexity to the imaging process.

Based on the observations discussed previously, our analysis revealed that on dip angles ranging from 0° to 5° and frequency ranges from 10 Hz to 50 Hz, the anhydrite interface was most clearly trackable in the migrated field data. However, even within these selected ranges, the identification of the anhydrite interface remained challenging, characterized by low resolution, and noise.

Our initial hypothesis, based on fluid flow from the salt dome cap to the mine entrance through the Röt-1 Anhydrite B unit, assumed that the anhydrite unit near the mine is saturated, leading to reduced velocity and density due to fluid presence or mineral alterations and fractures. However, the lack of geophysical parameters for this saturated unit in the vicinity of the mine poses limitations to our analysis.

Synthetic modeling revealed due to the presence of tuning effects, that the amplitude of the seismic event increases for near offsets but decreases for larger offsets approaching the critical angle; Additionally, due to the steep reflector geometry in the study zone, it is possible that minimal energy returned back to the surface or were not recorded in the vertical component. These phenomenon may contribute to the lower amplitude and challenging interpretation of the anhydrite event at dip angles greater than 5°, if the assumptions made in our study hold true. However, practical seismic behavior is more complex, involving effects of anisotropy, attenuation, and structural layering, which were not accounted for in our study.

Despite these limitations, our study provided insights into the seismic response of the anhydrite unit under varying dip angles and frequencies. When considering the preceding chapters, this study as a whole has enabled us to understand the seismic response to certain effects, such as the behavior of reflection and refraction coefficients of the anhydrite unit across various angles of incidence and their relationship when using base geophysical parameters versus reduced parameters. Furthermore it makes clear on the tuning effect and its influence on seismic interpretation, despite being limited by our simplified modeling approach. Understanding these complexities is crucial for improving seismic imaging and interpretation in similar geological settings. Further research incorporating more realistic seismic models and accounting for additional complexities (as the consideration of the seismic effects of the mine) is needed to refine our understanding of the seismic response in the study area.

Chapter 7

Conclusions

The seismic response in relation to the Röt-1 Anhydrite B layer in the Asse region has been examined in this study. Through synthetic modeling and analysis of field data, we aimed at getting a better understanding of the seismic signatures associated with this geological formation.

Taking into account the exploding reflector test, we could observe that it is possible to expect a zero-offset signal from the steep flank within a range of approximately 1000 meters south of ASSE Shaft 2. However, this signal would be faint due to the structural and geological complexity of the area, which results in multiple events, making it difficult to identify signals from the area of interest in the field data. Additionally, it is noted that the signal in the Vx component is stronger for the diping reflector events due to the polarization of the P-waves. Therefore, in such configuration x-component records would offer aditional information.

We observed that reducing geophysical parameters in the Anhydrite layer by 10% resulted in notable changes in seismic signals, particularly in amplitude and in low angles of incidence. However, the alterations in arrival time were minimal, and no significant waveform distortion was observed.

Due to its thickness of only 16 m here will be interference between the seismic responses of the top and base anhydrite that causes a tuning effect. The tuning effect is avoided by increasing the thickness of the layer (higher than 40 m), which makes it easier to distinguish between the seismic response of the top and lower surfaces. It is expected that the field data will exhibit tuning effects on the Röt-1 Anhydrite B layer in the ASSE model configuration.

The introduction of a perturbation within the anhydrite layer led to reduced amplitude and time shifts in seismic signals. Additionally, reflections from perturbation boundaries induced additional complexities in the waveform, known as the scattering effect. Nevertheless its amplitudes are lower.

The anhydrite interface was most clearly trackable within dip angles ranging from 0° to 5° and frequency ranges from 10 Hz to 50 Hz, according to our examination of the field data at different dip angles and frequencies. Even within these selected ranges, challenges in tracking the Anhydrite reflector remained challenging, characterized by low resolution, and noise.

The synthetic models help in our understanding of the various phenomena that might be present in the field data, even though they were not directly comparable with the field data.

Further studies are necessary to clarify all the phenomena present in the field data, considering that the present study was an initial approach to the problem and has limitations such as the lack of data to create more realistic models and the assumptions considered. Investigations on the influences of the mine chambers in the seismic data must be consider in further studies as well.

Bibliography

Bacon, M., Simm, R., and Redshaw, T. (2013). "Interpreting seismic amplitudes". In: *3-D Seismic Interpretation*. Cambridge University Press, pp. 120–154. DOI: 10.1017/cbo9780511802416.006.

BGE (2018). *Bericht zur Revisionskartierung (M 1:5.000) der Salzstruktur Asse im Bereich zwischen Groß Denkte und Klein Vahlberg*. Tech. rep. Salzgitter: BGE Bundesgesellschaft für Endlagerung mbH.

Bohlen, T. (2002). "Parallel 3-D viscoelastic finite difference seismic modelling". 28, pp. 887–899. URL: http://www.iamg.org/CGEditor/index.htm..

Brauer, A. (2017). *Statusbericht zum Bestand des Abbaus 3/658 in der Schachtanlange Asse II*. Tech. rep. BGE Bundesgesellschaft für Endlagerung mbH.

Castagna, J. P. and Backus Milo M. (1993). *Offset-Dependent Reflectivity – Theory and Practice of AVO Analysis*. Vol. 8. Society of Exploration Geophysicists.

Crase, E., Picat, A., Noble, M., Mcdonald, J., and Tarantola, A. (1990). "Robust elastic nonlinear waveform inversion: Application to real data". 55.5, pp. 527–538. URL: http://library.seg.org/.

De Paola, N., Faulkner, D. R., and Collettini, C. (2009). "Brittle versus ductile deformation as the main control on the transport properties of low-porosity anhydrite rocks". *Journal of Geophysical Research: Solid Earth* 114.6. ISSN: 21699356. DOI: 10.1029/2008JB005967.

Denham, L. R. (1984). "Seismic Interpretation". *Proceedings of the IEEE* 72.10.

Fanchi, J. R. (2010). "Geophysics". In: *Integrated Reservoir Asset Management*. Elsevier, pp. 71–88. DOI: 10.1016/B978-0-12-382088-4.00005-0. URL: https://linkinghub.elsevier.com/retrieve/pii/B9780123820884000050.

Fawad, M., Hansen, J. A., and Mondol, N. H. (Nov. 2020). "Seismic-fluid detection-a review". *Earth-Science Reviews* 210. ISSN: 00128252. DOI: 10.1016/j.earscirev.2020.103347.

Gärtner, G. (Feb. 2012). *Fließwege zutretender Salzlösungen im Grubengebäude der Schachtanlage Asse II*. Tech. rep. Fachbereich Sicherheit nuklearer Entsorgung, Projekt Asse, Fachgebiet SE 4.2 - Fachfragen.

Gassmann, F. (1951). "Über die Elastizität poröser Medien". *Naturforschende Gesellschaft in Zürich*. DOI: https://doi.org/10.1190/1.1437718.

Gauthier, O., Virieux, J., and Tarantola, A. (1986). *Two-dimensional nonlinear inversion of seismic waveforms: Numerical results*. Tech. rep. 7. URL: http://library.seg.org/.

Ge, Z., Pan, X., Liu, J., Pan, S., and Li, J. (2022). "Zoeppritz-equations-based amplitude variation with angle inversion for Russell fluid factor in a gas-bearing reservoir". *Journal of Petroleum Science and Engineering* 208. DOI: 10.1016/j.petrol.2021.109204.

Google (2024). *Google Earth*. URL: http://earth.google.de/.

GSF (1996). *Zusammenfassende Darstellung der Laugensituation am Standort Asse*. Tech. rep. Remlingen: GSF Forschungszentrum für Umwelt und Gesundheit GmbH – Forschungsbergwerk Asse.

Hente, B. (1997). *Geoelektrische Überwachung des Salzberwerks Asse Ergebniszusammenfassung*. Tech. rep. GSF Forschungszentrum für Umwelt und Gesundheit GmbH – Forschungsbergwerk Asse.

Hente, B. (2002). *Geoelektrische Messungen im Forschungsbergwerk Asse*. Tech. rep. GSF Forschungszentrum für Umwelt und Gesundheit GmbH – Forschungsbergwerk Asse.

Herron, D. (Jan. 2011). "Seismic Response". In: *First Steps in Seismic Interpretation*. Society of Exploration Geophysicists. ISBN: 9781560802808. DOI: 10.1190/1.9781560802938.ch2. URL: https://doi.org/10.1190/1.9781560802938.ch2.

Lehmann, P. (2016). *Zwischenbericht geophysikalischer Bohrlochradarmessungen zur Standorterkundung Abbau 3/658 in der Schachtanlage Asse II*. Tech. rep. Weimar: Bo-Ra-tec GmbH.

Linder, U. and Thoma, H. (1996). *Ergebnisbericht der ultraschallseismischen Messungen in der Kammer 2 des Forschungbergwerkes Asse*. Tech. rep. Sondershausen: Kali-Umwelttechnik GmbH Sodershausen.

Ludwig, R. J., Iturrino, G. J., and Rona, P. A. (1998). "Seismic velocity-porosity relationship of sulfide, sulfate, and basalt samples from the tag hydrothermal Mound". *Proceedings of the Ocean Drilling Program, Scientific Results* 158.

Nanda, N. C. (2021). *Seismic Data Interpretation and Evaluation for Hydrocarbon Exploration and Production*. Second. Springer International Publishing. ISBN: 978-3-030-75300-9. DOI: 10.1007/978-3-030-75301-6. URL: https://link.springer.com/10.1007/978-3-030-75301-6.

Naseer, M. T. and Asim, S. (2018). "Application of instantaneous spectral analysis and acoustic impedance wedge modeling for imaging the thin beds and fluids of fluvial sand systems of Indus Basin, Pakistan". *Journal of Earth System Science* 127.7. DOI: 10.1007/s12040-018-0997-1.

Naumann, D. and Rölke Christopher (2019). *Materialcharakterisierung von Versatzproben aus dem Abbau 3 auf der 658-m-Sohle*. Tech. rep. Leipzig: Institut für Gebirgsmechanik GmbH Leipzig.

Pollok, L., Saßnowski, M., Kühnlenz, T., Gundelach, V., Hammer, J., and Pritzkow, C. (2018). "Geological exploration and 3D model of the Asse salt structure for SE expansion of the Asse II mine". In: *Mechanical Behavior of Salt IX*, pp. 978–981. ISBN: 9783981410860.

Saeed, W., Zhang, H., Guo, Q., Ali, A., Azeem, T., Toqeer, M., Munawar, M. J., and Hussain, M. (2020). "An integrated petrophysical-based wedge modeling and thin bed AVO analysis for improved reservoir characterization of Zhujiang Formation, Huizhou sub-basin, China: A case study". *Open Geosciences* 12.1, pp. 256–274. DOI: 10.1515/geo-2020-0011.

Sass, I. and Burbaum, U. (2010). "Damage to the historic town of Staufen (Germany) caused by geothermal drillings through anhydrite-bearing formations". *ACTA CARSOLOGICA* 39.2, pp. 233–245.

Saßnowski, M., Pollok, L., Kühnlenz, T., Hammer, J., and Pritzkow, C. (2018). "Detailed petrographic and structural studies of salt rocks as basis for an internal geological 3D-model of the Asse salt structure (German Zechstein)". In: *Mechanical Behavior of Salt IX*, pp. 978–981. ISBN: 9783981410860.

Scheck, M., Bayer, U., and Lewerenz, B. (Jan. 2003). "Salt movement in the Northeast German Basin and its relation to major post-Permian tectonic phases - results from 3D structural modelling, backstripping and reflection seismic data". *Tectonophysics* 361 (3-4), pp. 277–299. ISSN: 00401951. DOI: 10.1016/S0040-1951(02)00650-9.

Scheck-Wenderoth, M. and Lamarche, J. (Mar. 2005). "Crustal memory and basin evolution in the Central European Basin System - New insights from a 3D structural model". *Tectonophysics* 397 (1-2 SPEC. ISS.), pp. 143–165. ISSN: 00401951. DOI: 10.1016/j.tecto.2004.10.007.

Sheriff, R. E. (1975). *Geophysical Prospecting*. Vol. 23. Chap. Factors Affecting Seismic Amplitudes, pp. 125–138.

Simm, R. and Bacon, M. (2014). *Seismic Amplitude An Interpreter's Handbook*. Cambridge University. ISBN: 978-1-107-01150-2.

Sortan, S. (2022). "Effects of seismic anisotropy and attenuation on first-arrival waveforms recorded at the Asse II nuclear repository". Maste r's thesis. Karlsruhe: Karlsruhe Institute of Technology.

Szymaniak, T. and Schäfer, M. (2002). "Geologisch-tektonische Kartierung der Salzstruktur Asse im Subhercynen Becken". Diplom. Clausthal-Zellerfeld: Technische Universität Clausthal.

Tarantola, A. (1984). *Inversion of seismic reflection data in the acoustic approximation*. Tech. rep. 8, pp. 1259–1266. URL: http://library.seg.org/.

Trela, J., Massaka, V., Potepa, P., Bilgili, F., Gärtner, G., and Teichmann, L. (2021). *Quantum nodal system-Asse 3D survey success story*. DOI: 10.3997/1365-2397.fb2021003.

Tucker, P. M. and Yorston, H. J. (1973). *Pitfalls in seismic interpretation*. Ed. by J. C. Hollister. Society of Exploration Geophysicists, p. 50. ISBN: 0931830117.

Wolff, P. (2021). *Hohlraumbilanz 2020 für die Schachtanlage Asse II und Kalkulation der Volumina zur Umsetzung der Maßnahmen zur Konsequenzenminimierung (Notfallplanung)*. Tech. rep. BGE Bundesgesellschaft für Endlagerung mbH.

Zivar, D., Foroozesh, J., Pourafshary, P., and Salmanpour, S. (2019). "Stress dependency of permeability, porosity and flow channels in anhydrite and carbonate rocks". *Journal of Natural Gas Science and Engineering* 70. DOI: 10.1016/j.jngse.2019.102949.

Zoeppritz, K. (1919). "Über Reflexion und Durchgang seismischer Wellen durch Unstetigkeitsflächen". *Nachrichten von der Gesellschaft der Wissenschaften zu Göttingen, Mathematisch-Physikalische Klasse*, pp. 66–84.

Zong, J., Stewart, R. R., Yang, J., Dyaur, N., and Wo, Y. (2023). "Investigating seismic mode conversions from an ultra-high-velocity caprock by physical modelling, numerical simulations and a Gulf of Mexico salt proximity VSP survey". *Geophysical Journal International* 234.2, pp. 1430–1446. DOI: 10.1093/gji/ggad151.

Appendix A

Software

- Shearwater Reveal, with an academic license (Shearwater GeoServices Software, Inc., 2023)
- SOFI2D (Bohlen et al., 2016): 2D finite-difference forward modeling
- Seismic Unix (Center forWave Phenomena, Colorado School of Mines)
- MATLAB, with an academic license (MATLAB, 2023)
- Python
- Overleaf, with a Professional KIT campus license

Acknowledgments

I would like to express my deepest gratitude to Prof. Dr. Thomas Bohlen for his invaluable mentorship, guidance, and for involving me in this exciting project. I would like to thank the BGE team, with special thanks to Maximilian Scholze, for their remarkable collaboration and access to essential data during this project. Their professionalism, cooperation, and willingness to share knowledge have greatly enriched my research experience. I would like to express my gratitude to Prof. Dr. Stefan Buske from TU Bergakademie Freiberg for serving as the Co-supervisor of this thesis.

A heartfelt thank you to the Applied Geophysics work group, particularly Lars Houpt and Thomas Hertweck, for their continuous support, technical assistance, and engaging discussions. Their expertise and camaraderie have truly enhanced the quality of my research. I also extend my appreciation to all my fellow students, with whom I have shared countless memorable moments and stimulating academic discussions. This adventure has been made even more rewarding by your companionship.

Lastly, I would like to dedicate a special thank you to my mother, father, and sister, whose unwavering support, love, and encouragement have been my pillar of strength throughout my academic pursuits. Your belief in me has been a source of inspiration, and I am forever grateful for your unconditional support.

This thesis would not have been possible without the contributions and support of each individual mentioned above. Thank you for being an integral part of my work.